

Dynamics of Gravitational Waves in 3D: Formulations, Methods, and Tests

Peter Anninos⁽¹⁾, Joan Massó^(1,2), Edward Seidel^(1,3), Wai-Mo Suen^(1,4,5), and Malcolm Tobias⁽⁴⁾

⁽¹⁾ *National Center for Supercomputing Applications, 605 E. Springfield Ave., Champaign, Illinois 61820*

⁽²⁾ *Department of Physics, Universitat de les Illes Balears, Palma de Mallorca E-07071, Spain*

⁽³⁾ *Department of Physics, University of Illinois at Urbana-Champaign*

⁽⁴⁾ *McDonnell Center for the Space Sciences, Department of Physics, Washington University, St. Louis, Missouri 63130*

⁽⁵⁾ *Physics Department, Chinese University of Hong Kong, Shatin, Hong Kong.*

(September 18, 2018)

Abstract

The dynamics of gravitational waves is investigated in full 3+1 dimensional numerical relativity, emphasizing the difficulties that one might encounter in numerical evolutions, particularly those arising from non-linearities and gauge degrees of freedom. Using gravitational waves with amplitudes low enough that one has a good understanding of the physics involved, but large enough to enable non-linear effects to emerge, we study the coupling between numerical errors, coordinate effects, and the nonlinearities of the theory. We discuss the various strategies used in identifying specific features of the evolution. We show the importance of the flexibility of being able to use different numerical schemes, different slicing conditions, different formulations of the Einstein equations (standard ADM vs. first order hyperbolic), and different

sets of equations (linearized vs. full Einstein equations). A non-linear scalar field equation is presented which captures some properties of the full Einstein equations, and has been useful in our understanding of the coupling between finite differencing errors and non-linearities. We present a set of monitoring devices which have been crucial in our studying of the waves, including Riemann invariants, pseudo-energy momentum tensor, hamiltonian constraint violation, and fourier spectrum analysis.

PACS numbers: 04.30.+x, 95.30.Sf, 04.25.Dm

I. INTRODUCTION

This paper is the first in a series of papers in which we numerically study gravitational waves in 3+1 dimensions. The systems studied range from weak gravitational waves with various symmetries, to fully general and highly nonlinear waves. We study the dynamical evolutions of the waves and the interactions between waves. That is, we investigate the dynamics of spacetime in its pure (vacuum) form, a subject that is important for theoretical, observational, and technical reasons. This area of research is for the most part uncharted territory due to its mathematical complexity and the need for large scale computational resources that have not been available previously. The general behavior of three-dimensional (3D) strong gravitational waves, including for example gravitational geons and the formation of singularities, is unknown. Previous analytic and numerical work on pure gravitational wave spacetimes, done in one or two spatial dimensions, has led to many interesting results, such as the formation of singularities from colliding plane waves [1–5] or the formation of black holes by imploding axisymmetric gravitational waves [6] and the existence of critical behavior in such systems [7]. These discoveries raise interesting questions about waves in more general 3D spacetimes. Yurtsever has proposed conjectures concerning the criteria for the formation of singularities from wave packets with finite extension in all 3 directions [4,5]. These conjectures, together with the global structure and local behavior of the singularities so formed, if indeed they can be formed, remains to be investigated. These questions call for a full 3D study.

Gravitational waves are also about to open up a fundamentally new area of astronomical observation: gravitational wave astronomy. A new generation of interferometric [8] and bar detectors [9] should detect waves for the first time near the turn of the century. Even though any observed waves are expected to have weakened by the time they reach Earth, they are likely to have been generated in regions with strong, highly dynamical and nonlinear gravitational fields. It is therefore essential to be able to study waves accurately in both the strong and weak field regimes, as well as the long term secular behavior in the transitory

intermediate regimes. The study of pure wave spacetimes will aid us in developing numerical codes to study all three regimes with confidence in the numerical results.

These pure wave studies compliment our program to compute the evolution and the radiation from the coalescence of two black holes in decaying orbits. Because black hole and gravitational wave systems each present their own set of technical difficulties, we first study black holes and waves separately, and then combine them after the problematics of each system are identified and understood. In a separate paper [10] we have presented results for a pure single black hole spacetime (i.e. Schwarzschild) evolved in three-dimensional Cartesian coordinates, with essentially the same basic code as used here. In future papers we will present results from evolutions of distorted black holes, including both gravitational waves and black holes.

In this first paper we focus on examining the difficulties one encounters in evolving relatively low amplitude 3D gravitational waves in Cartesian coordinates, and on the strategies we developed to solve those problems. We begin with low amplitude waves, as one has better physical understanding of what should be happening in such cases. When the amplitude is very low, the evolution is linear and nothing interesting happens. What is more interesting is waves in the “near-linear” regime, the meaning of which will become clearer throughout the paper. Basically, we mean waves which show some nonlinear transient or secular effects that can be observed in our numerical study within the limit of the accuracy and time scale of the evolution that we can currently achieve. These effects could be due to (i) numerical errors (finite differencing errors) coupled with nonlinearity, (ii) coordinate effects due to nonlinearity, or (iii) nonlinear physics. [Of course there is also a (iv) that we have invested a lot of effort in making sure of its absence (an effort which is not discussed here), namely, coding errors]. In this first paper, our aim is to study (i) and (ii) instead of (iii). We find that there are indeed cases for which (i) and (ii) give rise to interesting features in the evolution, but have negligible nonlinear physical effects.

It is nontrivial to distinguish whether a feature is due to (i), (ii), or (iii). To make the distinction between these effects, we have implemented many monitors of the evolution,

e.g. Hamiltonian constraint, pseudo-energy-momentum tensor, curvature components and curvature invariants. We have the options of using different gauge and slicing conditions, different boundary conditions, different finite differencing schemes, with different orders of finite differencing. In addition to the codes that evolve the full 3-D nonlinear Einstein equations, we have developed other evolution codes for comparison, e.g., codes that evolve the linearized Einstein equations, and codes that evolve a scalar field equation that captures important features of the full Einstein equations. Most noteworthy is that we have developed two completely independent codes that are based on two very different analytic formulations of the full Einstein evolution equations. All simulations presented in this paper were run with both codes, and the results were compared in detail. It is important to point out that the two codes will not produce identical results. One code is based on a particular gauge choice where that gauge condition is assumed in the evolution equations, whereas the other code has the evolution equations in their completely general form. When a gauge is chosen it can only be kept to numerical error.

The first of these fully nonlinear codes, which we call the “G” (for General) code, is based on the standard 3+1 ADM [11] approach to numerical relativity. It has been written in a fully general way, without specializing the equations to any lapse or shift condition, and without any restrictions on symmetry or initial data. The second code, which we call the “H” (for Harmonic) code, is based on the first order, flux-conservative, hyperbolic formulation of the Einstein equations developed by Bona and Massó [12,13]. Different finite differencing and evolution schemes have been incorporated into both codes, as well as linearized versions of both formulations. All these different codes and options were essential in enabling us to sort out the effects (i)-(iv) mentioned above.

We discuss three types of testbeds in this paper. The first test we consider is a single plane symmetric wave packet, propagating in some arbitrary direction. This problem allows us to compare the dispersive and dissipative properties of the codes for waves propagating in different directions in the 3D Cartesian grid, and the resolution needed for a given desired accuracy.

The second type of test we consider is the collision of weak plane wave packets. The focus here is on an effect caused by a coupling between finite differencing errors and the nonlinearity of the evolution equations. It manifests itself as a drifting of the metric function in a region where the wave packet has crossed. We discuss in detail how the cause of this drift can be identified. We develop a scalar field equation which captures important features of the nonlinear evolution of the Einstein equations. Testbeds done with this equation have been crucial in this analysis. We propose that this scalar equation be used as a standard testbed for the numerical study of gravitational waves.

The third type of testbed is an imploding-exploding combination of quadrupole wave packets [14,15]. Besides analyzing the accuracy of the numerical evolution, the focus here is on the coupling between the motion of the coordinates and the nonlinearity of the Einstein equations. With geodesic slicing, this coupling manifests itself as a “dipping” of some metric functions at the center of the symmetry, at a time long after the implode-explode process. We study at what amplitude this phenomenon becomes observable. We report on the analysis carried out in confirming that this behavior is due solely to coordinate motion instead of truly nonlinear physics.

For all three types of testbeds, we have studied the evolution of initial data sets which satisfy the constraint equations to linear order, and for the third testbed, data that completely satisfies the constraints, obtained through the York’s formalism [16]. We have checked that the two kinds of initial data basically lead to the same kinds of evolution for the low amplitude waves studied in this paper, hence we do not discuss the two cases separately unless otherwise mentioned. Throughout the paper we restrict ourselves to time symmetric initial data for simplicity when solving for the initial value problem, which is not our major concern in this paper.

In this paper we use the convention of [17], in which $c = 1$ and, as we are studying vacuum spacetimes, G does not enter. The system has no intrinsic length scales except those set by the waves, e.g. wavelength.

This paper is separated into the following sections: Section II reviews the two different

codes we have developed, which are based on the two different analytic formulations of the Einstein equations. We also discuss the numerical methods used in these two codes. The different tests and comparisons of our codes are presented in Sections III-VI. Section III is on planewave packets. Section IV is on colliding packets. Section V discusses a nonlinear scalar field equation that is useful in analyzing the nonlinearity of the Einstein evolution equations. Section VI is on imploding-exploding quadrupole waves. Section VII is a brief discussion and conclusion.

II. BASIC FORMALISMS AND NUMERICAL METHODS

A. The Fully Nonlinear 3D Codes

We have developed two independent 3D codes to solve the fully nonlinear set of Einstein equations. As all tests presented in this paper are performed with both codes, this approach allows us to study systematically the effect of not only different numerical methods, of which we have tested several, but also different mathematical formulations of the equations.

1. The “G” code

The first code we present is the “G” code, where G stands for general. This code uses the standard 3+1 ADM formulation of the Einstein equations. It is general in the sense that it can be used with arbitrary slicing and spatial coordinate conditions. The general spacetime metric is of the form

$$ds^2 = (-\alpha^2 + \beta_i \beta^i) dt^2 + 2\beta_i dx^i dt + g_{ij} dx^i dx^j, \quad (1)$$

where α and β^i are the lapse function and shift vector respectively. Although the vacuum ADM equations are given in many papers, we again show them here so that one may compare them with a second formulation discussed below:

$$\partial_t g_{ij} = -2\alpha K_{ij} + \nabla_i \beta_j + \nabla_j \beta_i \quad (2)$$

$$\begin{aligned} \partial_t K_{ij} = & -\nabla_i \nabla_j \alpha + \alpha (R_{ij} + K K_{ij} - 2K_{im} K_j^m) \\ & + \beta^m \nabla_m K_{ij} + K_{im} \nabla_j \beta^m + K_{mj} \nabla_i \beta^m . \end{aligned} \quad (3)$$

Here ∇_i is the spatial covariant derivative, R_{ij} is the spatial Ricci tensor and K is the trace of the extrinsic curvature. While the code admits arbitrary kinematic conditions for α and β^i , in this paper we report only on results obtained with either geodesic slicing ($\alpha = 1$), maximal slicing or harmonic slicing for the lapse function, and zero shift vector. The maximal slicing lapse

$$\nabla^m \nabla_m \alpha = \alpha R , \quad (4)$$

is derived by taking the trace of (3) and setting $K = \partial_t K = 0$. The harmonic slicing condition for the lapse is derived imposing the harmonic condition on the time coordinate, leading to the evolution equation

$$\partial_t \alpha = -\alpha^2 K \quad (5)$$

where the initial value for the lapse is completely arbitrary.

It is also appropriate to introduce the Hamiltonian constraint:

$$h = R + K^2 - K_{ij} K^{ij} = 0 . \quad (6)$$

Although the evolution equations theoretically preserve the Hamiltonian constraint in time, this is not generally so in numerically constructed spacetimes. Discretization effects accumulate over time, which can lead to violations of the Hamiltonian constraint. The quantity h defined in Eq. (6) therefore offers a means of monitoring errors introduced in the numerical evolution.

Equations (2) and (3) are expanded in a 3D Cartesian coordinate system and coded in FORTRAN using MACSYMA scripts written originally by David Hobill. More details of this code are provided in Ref. [10], where it was applied to black hole spacetimes.

An important point to stress is that the equations have not been specialized in any way. All gauge degrees of freedom are left general, so that any shift and lapse conditions may easily be imposed. On the other hand, this implies that if a particular gauge choice is used for the initial data (i.e., a diagonal form of the metric or a traceless extrinsic curvature), the equations themselves are not specialized to that gauge, and this allows for the possibility that the gauge condition may not be strictly satisfied after some evolution due to numerical errors. We view it as an important strength of this code, as it opens up the possibility of investigating the stability of various gauge choices.

This code is sufficiently flexible that it allows different evolution schemes to be implemented easily, and we have developed the following two numerical schemes that are second order accurate in space and time: a staggered leapfrog with half time step extrapolation, and a “MacCormack-like” predictor-corrector method. An essential difference between them is that in the MacCormack scheme, all quantities are centered on the same time slices at all times, and therefore no extrapolations or averages are needed to get quantities that are properly centered. The leapfrog scheme has the 3-metric and extrinsic curvature variables offset by $1/2$ time slice, so that although the main time derivative terms are properly centered, a number of important terms in the evolution equations require extrapolations or averaging in time. The details of these methods have been published elsewhere [see e.g. Ref. [18]], and so we will not present them here (however see Section V where we apply these methods to a simplified model problem).

2. The “H” code

The second code (“H”) is based on the work of Bona and Massó [13] that casts the Einstein equations in an explicitly first order, flux conservative, hyperbolic form. In this paper we present the first results of this new formulation to gravitational wave spacetimes.

The general metric is also of the form (1) and spacetime coordinates are chosen such that the shift vector vanishes. It was shown in Ref. [13] that if one restricts the lapse to

the harmonic slicing (5), one can write the Einstein evolution equations as a hyperbolic first order system of balance laws that in vacuum takes the form:

$$\partial_t g^{ij} = Q^{ij} \quad (7)$$

$$\begin{aligned} \partial_t \left[\frac{\sqrt{g}}{\alpha} Q^{ij} \right] - \partial_k \left[\alpha \sqrt{g} \left(D^{kij} + g^{ki} g^j + g^{kj} g^i \right) \right] \\ = \frac{\sqrt{g}}{\alpha} Q^{ik} Q_k^j - 2\alpha \sqrt{g} \left[g^{ikl} g_{kl}^j + L^i L^j - g^i g^j \right] , \end{aligned} \quad (8)$$

$$\partial_t \left[D_k^{ij} \right] - \partial_k \left[Q^{ij} \right] = 0 , \quad (9)$$

$$\partial_t g^i = Q_k^k L^i - 2Q_j^i L^j + g_{jk}^i Q^{jk} . \quad (10)$$

The Q^{ij} quantities are proportional to the extrinsic curvature. Note that all the sources (on the RHS) account for the nonlinear terms and that the three-dimensional ricci does not appear as it has been split into its transport part and its nonlinear source. The connection coefficients g_{jk}^i are constructed from the first derivatives of the metric

$$D_k^{ij} = \partial_k g^{ij} . \quad (11)$$

These derivatives are evolved using Eq. (9). Eq. (11) is only used in the initial slice. Similarly, the derivatives of the lapse are used on the initial slice to construct $L^i = \partial^i \ln \alpha$ and to derive the initial values of the momentum constraint related variables:

$$g^i = \frac{1}{2} g_{jk} D^{ijk} - D_k^{ki} - L^i . \quad (12)$$

These variables are evolved using Eq. (10) while Eq. (12) is used to compute the L^i during the evolution.

At present this code is restricted to use the harmonic lapse condition with a vanishing shift, although recent work [19] shows that the same first order, flux conservative, hyperbolic form can be maintained with a wider class of slicing conditions. Results from a code developed with this more recent formulation of the equations will be presented elsewhere.

Standard operator splitting techniques allows for the principal part of the system to be treated as a flux conservative first order system. This kind of system is well known

in Computational Fluid Dynamics (CFD), where a wide choice of modern and standard numerical methods have been developed. In this case a flux conserving MacCormack method is used for the principal part of the evolution system. Note that this is a *true* MacCormack method, developed for truly first order systems of equations, and not the “MacCormack-like” predictor-corrector method used in the “G” code (again see Section V where we apply these methods to a simplified model problem).

B. The Linearized 3D Codes

The discussion above was centered on the two codes we have developed to solve the fully nonlinear Einstein equations. In order to help sort out linear from nonlinear effects and physical from numerical effects, we have also developed linearized versions of both the “G” and “H” codes. Both codes have been written in such a way that subroutine calls can be made to solve either the full Einstein equations or the linearized versions. In this way all numerical algorithms not associated with the expressions themselves are identical and we can be sure that effects we see are related only to the linearization process, and not to slight differences in coding or numerical techniques that might otherwise arise if different codes were developed.

The general linearized version of the ADM Equations (2) and (3) are long and unwieldy to write out explicitly. The task is simpler for the harmonic formulation, as it amounts to linearizing the principal part and setting all the nonlinear sources on the RHS of the equations (7)–(10) to zero. In any case, a simplified set of linearized ADM equations results when we set $\beta^i = 0$ and $\alpha = \text{constant}$ to second perturbative order. We will present these equations here to provide a framework for obtaining analytic solutions to the Einstein equations at first perturbative order for weak waves. However, we stress that it is the general form of the linearized equations that we solve numerically, and not the specialized equations presented below.

The perturbation expansion can be written in the form

$$g_{ij} = g_{ij}^{(0)} + \epsilon g_{ij}^{(1)} , \quad (13)$$

$$K_{ij} = K_{ij}^{(0)} + \epsilon K_{ij}^{(1)} , \quad (14)$$

where $\epsilon \ll 1$ is the smallness parameter and the superscripts (0) and (1) refer to the 0th and 1st order solutions. Assuming a Minkowski background spacetime such that

$$g_{ij}^{(0)} = \text{diag} [1, 1, 1] , \quad (15)$$

$$K_{ij}^{(0)} = 0 , \quad (16)$$

and $\alpha = 1$, the 0th order equations are satisfied trivially and the resulting linearized ADM equations become

$$\partial_t g_{ij}^{(1)} = -2\alpha K_{ij}^{(1)} , \quad (17)$$

$$\partial_t K_{ij}^{(1)} = \alpha R_{ij}^{(1)} . \quad (18)$$

If we make the further assumption of a diagonal 3-metric which is a function only of the single coordinate z , the nonvanishing components of the Ricci curvature tensor are

$$R_{xx}^{(1)} = -\frac{1}{2} g_{xx,zz}^{(1)} , \quad (19)$$

$$R_{yy}^{(1)} = -\frac{1}{2} g_{yy,zz}^{(1)} , \quad (20)$$

$$R_{zz}^{(1)} = -\frac{1}{2} \left(g_{xx,zz}^{(1)} + g_{yy,zz}^{(1)} \right) . \quad (21)$$

Eqs. (17) and (18) then reduce to three equations for the diagonal metric components

$$\partial_t^2 g_{xx}^{(1)} = \alpha^2 g_{xx,zz}^{(1)} , \quad (22)$$

$$\partial_t^2 g_{yy}^{(1)} = \alpha^2 g_{yy,zz}^{(1)} , \quad (23)$$

$$\partial_t^2 g_{zz}^{(1)} = \alpha^2 \left(g_{xx,zz}^{(1)} + g_{yy,zz}^{(1)} \right) . \quad (24)$$

The Hamiltonian constraint (6) reduces to

$$R^{(1)} = - \left(g_{xx,zz}^{(1)} + g_{yy,zz}^{(1)} \right) = 0 . \quad (25)$$

Analytic solutions to equations (22) — (25) are discussed in Section III 1.

III. CODE TEST 1 - SINGLE WAVE PACKET

In this section we present a set of code tests involving the propagation of plane wave packets traveling in one dimension. We evolve these plane wave packets with our full 3D codes to test wave propagation in all three orthogonal directions (x , y and z) independently and to look for any asymmetries in the evolution for debugging purposes. These results can then be compared with the propagation of waves along some arbitrary oblique angle that is not parallel to any coordinate axis, which tests the accuracy of resolving arbitrary waves on our rectangular grid. Since for such waves we can use fewer grid zones in the transverse directions than in the longitudinal directions, this allows us to perform tests without severely being constrained by available computer memory as in the full 3D case. We have checked in all cases we have studied that for very low amplitudes, the evolutions obtained by the full 3D non-linear codes are indistinguishable from those obtained by the linearized codes described in Section II above.

1. linearized solution

A solution to the perturbation evolution equations (22) — (24) that is consistent with the Hamiltonian constraint (25) can be given by

$$ds^2 = -dt^2 + (1 + f(t, z))dx^2 + (1 - f(t, z))dy^2 + dz^2, \quad (26)$$

with $f(t, z)$ satisfying the linear wave equation

$$\partial_t^2 f(t, z) = \partial_z^2 f(t, z) \quad (27)$$

for linearized plane waves propagating in the z direction [17]. Setting $g_{xx}^{(1)} = -g_{yy}^{(1)}$ gives the transverse-traceless (TT) gauge in which the wave amplitudes are purely spatial, traceless and transverse to the propagation direction. The metric (26) describes gravitational waves with a single mode of polarization e_+ .

We will study the solutions of a gaussian shaped wave packet with

$$f(t, z) = \left[A_R e^{-(2\pi(t-z-a)/\sigma)^2} \cos\left(\frac{2\pi}{\lambda}(z-t)\right) + A_L e^{-(2\pi(t+z-a)/\sigma)^2} \cos\left(\frac{2\pi}{\lambda}(z+t)\right) \right]. \quad (28)$$

The parameters A_R and A_L represent the amplitudes of waves traveling to the right and left, respectively, with a gaussian shape of width σ and centered at $z = \pm a$ at $t = 0$. λ is the wavelength of the gaussian modulated oscillations. If $\sigma \gg \lambda$, equation (28) represents a pure sinusoidal mode and for $\sigma \ll \lambda$, a pure gaussian packet. By changing the metric functions appropriately, it can just as easily describe a wave traveling along the x - or y -axes, or be generalized to a wave traveling in some arbitrary direction.

We note that the harmonic slicing condition (5) is consistent with geodesic slicing ($\alpha = 1$) to first order as long as the traceless gauge ($K = 0$) is maintained. Hence the linearized solutions presented above apply to the hyperbolic formulation with no modifications.

2. Convergence studies

In Fig. 1 we show the evolution of the plane symmetric waves defined by (26) and (28) with shape parameters $\sigma = 2.0$, $\lambda = 1.0$, $A_L = 0.00001$, $A_R = 0$ and $a = 3$. This run is typical of the resolution and time scales for most of our evolutions. The wave is shown at $t = 0$, $t = 3$, and $t = 6$. The evolution is with $\Delta x = \Delta y = \Delta z = 0.025$.

In Fig. 2 we evolve the initial data above, but with $a = 0$ and periodic boundary conditions. This allows the waves to continue to propagate through the computational domain, allowing us to evolve the wave for much longer times, without increasing the grid size. The waves are shown at three different times $t = 0$, 10 and 20. Since the wave propagation speed is unity and the outer grid boundaries are set at $z = \pm 5$, the displayed profiles correspond to the wave positioned at the grid center. At $t = 20$, the wave has propagated across the extent of the entire grid twice. Data for the same sequence of times are presented for three different spatial resolutions with grid spacing $\Delta x = 0.1$, 0.05 and 0.025 for both the ‘‘G’’ and ‘‘H’’ codes. The ‘‘G’’ code evolutions are performed with the standard leapfrog scheme

with half step extrapolation. A full MacCormack scheme is used in the “H” code.

At the coarser resolutions, the waves disperse due to numerical discretization effects. These effects are more evident in the “H” code evolutions of Fig. 2a. At higher resolutions, the two codes yield comparable results that reproduce accurately the solution (28), which is represented by the initial data at $t = 0$.

In Fig. 3 we plot the RMS error, where the error is defined as

$$E = \left| \frac{g_{xx}^{(a)} - g_{xx}^{(n)}}{g_{xx}^{(a)}} \right|, \quad (29)$$

as a function of the grid resolution Δx . Here $g_{xx}^{(a)}$ is the linear analytic solution (28) and $g_{xx}^{(n)}$ is the numerical solution from the nonlinear codes. [As the amplitude of the wave is low, the analytic solution to the linearized equations Eq. 28 is basically the same as the exact nonlinear solution, and E in Eq. (29) represents the error in this sense.] The boxes (circles) are the “G” (“H”) code results. We find the error scales as $E \sim \Delta x^\alpha$ with $\alpha \sim 2$ as expected for fully second order methods. In all our simulations, the timesteps have been chosen to be proportional to the grid spacing $\Delta t = C\Delta x$, with $C < 1/\sqrt{3}$ to satisfy the 3D Courant stability condition. We use $C = 0.2$ for both codes in the calculations presented in this section. We find that in order to keep errors below $E < 10^{-4}$ at $t = 10$, it is necessary to resolve a wavelength with 20 grid points with the “G” code and 40 using the “H” code. For waves traveling along the diagonal, we find the resolution needs to be increased by approximately $\sqrt{2}$ to get the same error as when the wave is traveling along an axis, as expected.

By looking at the solutions in Fourier space, we can see numerical effects not clearly evident in Fig. 2. In Fig. 4 we plot the Fourier transform of $g_{xx} - 1$ at three different times for the intermediate resolution case with $\Delta x = 0.05$. The wavelength $\lambda = 2\pi/k = 1$, corresponding to the dominant mode, is resolved with ~ 20 grid cells at this resolution. We find, in general, that amplitude errors due to numerical dissipation dominate over phase errors for typical resolutions, and that the MacCormack method used in the “H” code is significantly more dissipative and dispersive than the leapfrog method of the “G” code.

Again, we stress that this is what we expect from the mathematical properties of their respective finite differencing operators.

As another test of the code, we monitor the Riemann curvature invariants [20]. It is known [20] that spacetimes containing only plane-fronted gravitational waves with parallel rays (pp waves) are of the Petrov classification type N and have vanishing invariants. We therefore expect (at least to linear order at which the metric (26) satisfies Einstein's equations) both curvature invariants I and J to vanish. The invariant I is plotted in Fig. 5 at three different resolutions to see that it is indeed converging to zero.

IV. CODE TEST 2 - COLLIDING WAVES

The propagation of plane symmetric waves discussed in the previous section allows many aspects of the codes to be tested, including the dispersive and dissipative nature of the various numerical schemes. Here we consider the collision of two identical plane wave packets. In such cases one expects to find nonlinear effects, even for vanishingly small amplitude wave packets. In fact, it is known that when two plane symmetric waves collide when traveling through an otherwise flat background, a curvature singularity is generated in the region where the waves cross due to the focusing effect of the waves [1]. Such a singularity gets generated even for arbitrarily weak waves, only the singularity will emerge at a later time.

In Figs. 6a-e we show an evolutionary sequence of a wave packet collision at the four times $t = 0, 3, 6$ and 9 for moderately resolved grids with $\Delta x = 0.05$ for Figs.a-d and $\Delta x = 0.025$ for Fig.6e. The initial data is of the form of Eq. (28) with the same parameters as the single wave packets in the previous section except now $a = 3$, and $A_L = A_R = 0.025$ so that the data set consists of two wave packets centered at $z = \pm 3$. First the two waves approach each other from their initial configurations at $t = 0$, collide at $t = 3$, and propagate to their original centered locations at $t = 6$.

Notice that in the “G” code after the collision there is a remnant left behind the waves. This remnant, shown clearly in Fig. 6a, grows in time. For waves with smaller amplitude,

this remnant is smaller initially, but grows to a large value at late times.

To test if the remnant in Fig. 6a is a nonlinear effect, in particular, if it is related to the singularity due to the focusing effect, we evolved the same initial data set using the *linearized* evolution equations. With linear evolution, no focusing is possible. The results are displayed in Fig. 6b. There is no remnant in the solutions for colliding linear plane waves. In view of this, one might be tempted to conclude that the remnant in case(a) is due to nonlinear physics. In fact, we will show this is not the case.

In Fig. 6c we show results from a “G” code simulation using the same initial data and resolution but with the MacCormack scheme. The remnant is greatly reduced. We also show in Fig. 6d the equivalent simulation performed with the “H” code. Here we see similar behavior as the waves approach and collide. However, after the collision we see that the remnant is nearly nonexistent, and it does not grow appreciably over the time scale of the run. Clearly the different numerical methods produce different results in the evolution. Finally, in Fig. 6e we show the same simulation with the fully nonlinear “G” code as before in Fig. 6a, but now with twice the resolution. In this case all other features are quite similar, but the remnant is now reduced significantly in amplitude. If we again double the resolution we will see the remnant reduced even further. We conclude that the remnant observed in Fig. 6a is a numerical artifact dependent on the numerical method and grid resolution.

So this remnant is *not* related to the singularity caused by the focusing effect. On the other hand, we know that there must be a singularity at a later time; how does it manifest itself? We note that the weaker the amplitude of the wave, the later in time the singularity will form. Based on the colliding packet study in Refs. [4] and [5], we expect that the singularity will develop at a time

$$t \sim \frac{\lambda^2}{(2\pi)^2 \sigma A^2} \quad (30)$$

after the collision. Where λ is the characteristic wavelength, σ is the characteristic width of the packet, and A is the characteristic amplitude of the packet. For the case here, with $\lambda \sim 1$, $\sigma \sim 1$, and $A \sim 10^{-2}$, we expect the singularity to appear at $t \sim 250$, which is

far beyond any evolutions shown here. In fact it is well beyond any time we can accurately evolve to with our present computer resources. It is tempting to make the singularity appear earlier by increasing the amplitude of the waves, so that the onset of the singularity can be studied. We have resisted the temptation to do this here, mainly because such a study is out of the scope of this paper. Another reason for not including this study in the paper is that, for a larger amplitude wave, one has to solve the initial constraints to higher order. With the planar symmetry, the non-linear effect of the wave will introduce a long length scale variation in the metric, which causes a coordinate singularity at some spatial location on the initial slice, and hence requires special treatment.

V. A MODEL NONLINEAR PROBLEM

To investigate the cause of the “remnant” in the nonlinear evolutions, we have developed a simplified model problem containing a single scalar field that exhibits similar behavior as the fully nonlinear Einstein equations.

We arrive at this nonlinear model by starting with the metric (26) used in the previous studies. However, now we keep the nonlinear terms in the ADM evolution equations (2) and (3). These lead to the evolution equation for $f(t, z)$

$$\partial_t f = \Pi , \tag{31}$$

$$\partial_t \Pi = f_{,zz} + \frac{\Pi^2 - (f_{,z})^2}{1 - f^2} . \tag{32}$$

Together, Eqs. (31) and (32) become

$$f_{,tt} - f_{,zz} = \frac{(f_{,t})^2 - (f_{,z})^2}{1 - f^2} . \tag{33}$$

When the order f^2 term on the R.H.S. is negligible, Eq. (33) reduces to the standard wave equation Eq. (27). Our aim here is to investigate the relation between this f^2 term and the numerical schemes used for the evolution. We note that the solution of Eq. (33) does not generate a solution of the Einstein equations as the resulting metric does not satisfy the constraint equations.

We have investigated this model equation using several different finite difference methods that closely parallel those used in the “G” and “H” codes. Here we will present results for the two methods used in the “G” code; staggered leapfrog with 1/2 time step extrapolation and a MacCormack-like predictor corrector scheme with no extrapolation.

For a full understanding of the effect, we give the complete discretized equations, first in the leapfrog scheme

$$f_j^{n+1} = f_j^n + \Pi_j^{n+1/2} \Delta t \quad (34)$$

$$\Pi_j^{n+3/2} = \Pi_j^{n+1/2} + \left[(f_j^{n+1})_{,zz} + \frac{(\Pi_j^{n+1})^2 - ((f_j^{n+1})_{,z})^2}{1 - (f_j^{n+1})^2} \right] \Delta t , \quad (35)$$

where the superscript n denotes the time level, and subscript j tracks the spatial position. f and its time derivative Π are staggered by a half step in time with respect to each other. Note that in updating the auxiliary variable Π from time $n + 1/2$ to $n + 3/2$, we need Π^{n+1} , but in the standard leapfrog scheme this auxiliary variable only exists on the half time steps. We approximate this value by extrapolating data from the previous two time steps

$$\Pi^{n+1} = \frac{3}{2} \Pi^{n+1/2} - \frac{1}{2} \Pi^{n-1/2} . \quad (36)$$

In the MacCormack scheme, we first solve the predictor step for the intermediate variables \tilde{f} and $\tilde{\Pi}$

$$\tilde{f}_j^{n+1} = f_j^n + \Pi_j^n \Delta t , \quad (37)$$

$$\tilde{\Pi}_j^{n+1} = \Pi_j^n + \left[(f_j^n)_{,zz} + \frac{(\Pi_j^n)^2 - ((f_j^n)_{,z})^2}{1 - (f_j^n)^2} \right] \Delta t , \quad (38)$$

followed by the corrector step

$$f_j^{n+1} = \frac{1}{2} \left[\tilde{f}_j^{n+1} + f_j^n + \tilde{\Pi}_j^{n+1} \Delta t \right] , \quad (39)$$

$$\Pi_j^{n+1} = \frac{1}{2} \left[\tilde{\Pi}_j^{n+1} + \Pi_j^n + \left((\tilde{f}_j^{n+1})_{,zz} + \frac{(\tilde{\Pi}_j^{n+1})^2 - ((\tilde{f}_j^{n+1})_{,z})^2}{1 - (\tilde{f}_j^{n+1})^2} \right) \Delta t \right] . \quad (40)$$

In this scheme, all variables are centered at the same time step at the completion of both predictor-corrector updates.

Results for the collision of two wave packets are shown in Fig. 7a. The initial data is given by Eq. (28) with parameters $\sigma = 1$, $A_L = A_R = 0.1$, and $a = 3$. We also set $\lambda \rightarrow \infty$ so that the initial data is a pure gaussian wave packet without sinusoidal oscillations. All calculations presented here were run at the same grid resolution of $\Delta x = 0.05$. Although the leapfrog and MacCormack schemes both perform well on the standard linear wave equation, they behave quite differently on this nonlinear test problem. In Fig. 7b we zoom in on the flat central portions of the afterwake. Although only the results from the leapfrog evolution are shown, we see a similar drift with the MacCormack-like evolution, although the drift is orders of magnitude smaller.

To understand these drifts, we note that under the approximation $f \ll 1$ and $f_{,z} = 0$, which are clearly appropriate in the region of the drift, Eq. (33) reduces to

$$f_{,tt} = f_{,t}^2 \quad (41)$$

which has a solution

$$f(t) = -\ln(c_1 t + c_2) \quad (42)$$

where c_1 and c_2 are arbitrary constants. To verify that the drifts are really of this form, we look at the origin after the waves pass through each other and then plot the quantity $e^{-f} - 1$ versus time. The results for the two different numerical methods are shown in Fig. 8 for $\Delta x = 0.05$, and indeed, we see straight lines. The constants c_1 and c_2 in Eq. (42) can be read out from the slopes and intercepts of these curves. For this case, we find the MacCormack scheme has a much smaller drift rate with $c_1 = 1.4 \times 10^{-7}$ and $c_2 = 1.0$, as compared to the leapfrog scheme with $c_1 = -9.8 \times 10^{-5}$ and $c_2 = 1.0$. Just as in the full “G” code, the remnant amplitude gets smaller as one goes to higher and higher resolution. We find that the drifting solution converges away with rates 3.86 and 3.49 for the leapfrog and MacCormack-like methods respectively. Here we are just using the three values of c_1 at different resolutions to calculate the convergence rate α

$$\alpha = \frac{c_1(\Delta x = 0.05) - c_1(\Delta x = 0.025)}{c_1(\Delta x = 0.025) - c_1(\Delta x = 0.0125)}. \quad (43)$$

(We note that this unstable mode can also be excited by a single wave packet and appears in the tail after the wave passes some region.)

The drifts shown in this section for the evolution of Fig. 8, and in the previous section for the evolution of the full Einstein equations are now readily understood: The nonlinear evolution equations contain unstable modes. We note that this is not in contradiction to the expectation that the Einstein equations are stable for weak waves (weak perturbations of the flat spacetime). It is the constraint equations that rule out these unstable modes. In our free evolution code the constraint equations are not enforced. This allows the unstable modes to develop after they are excited by the numerical errors in the evolution. Exactly which mode will be excited most and the amount it is excited depends on the details of the numerical scheme. Here we see that the leapfrog scheme as given by (31) and (32) is more prone to the excitation of the unstable modes of the form (42). This is because the extrapolation (36) leads to inaccuracies that ruin the exact cancellations on the RHS of (33) in the trailing edge of the wave. We have further analyzed this point by (i) studying the unstable mode given by (42) for the case of a single wave packet, in which the same phenomena occurs; (ii) using a different extrapolation scheme in place of that given by (36), e.g. one based on a second-order Taylor expansion; and (iii) by reducing the Courant factor by a factor of 10. We find that increasing the accuracy of the extrapolation in Eq. (36) leads to slightly better results as far as the unstable drift is concerned, but none of the methods we tried compare favorably to the predictor-corrector schemes which require no extrapolation.

To confirm that this is the same phenomenon as we observed in the Einstein equations, we have verified that the drift in the wave remnants follows the form (42). For similar grid parameters we find similar values for the coefficients: $c_1 = -1.6 \times 10^{-4}$ and $c_2 = 1.0$ for the leapfrog method and $c_1 = 7.9 \times 10^{-7}$ and $c_2 = 1.0$ for MacCormack-like method. Again, the drifting solution is orders of magnitude smaller for the MacCormack-like method.

VI. CODE TEST 3 - PURE QUADRUPOLE WAVES

The third test problem on the construction of general relativistic spacetimes we discuss is the quadrupole waves [14,15] with an imploding—exploding nature. We use the quadrupole waves to test the 3D propagation of low amplitude waves in our 3D Cartesian codes. As these solutions represent quadrupole waves, they provide standards against which we can compare the codes’ ability to evolve waves which do not conform to the rectangular geometry of Cartesian grids. In the following two subsections, we study these waves first in linear settings and then with full nonlinearity.

A. Quadrupole waves satisfying the IVP to linear order

Linearized quadrupole waves (Teukolsky waves) have been given for both even and odd parity solutions and the independent azimuthal modes in Ref. [15] . Due to the length of these expressions, we do not write out the solutions here. The axisymmetric version of these solutions has been used as a testbed for a number of axisymmetric evolution codes (see, for example, Ref. [21]).

In our first set of numerical tests, the initial data is taken to be essentially the form given by [15], but modified to be time symmetric and contain an ingoing and outgoing wave in such a combination as to make them regular everywhere in spacetime [14]. We note that as small amplitude waves on the Minkowski background, the constraint equations are trivially satisfied to first order, but violated to second order. Quadrupole waves that satisfy the full constraint equations will be studied in the next section.

We study the evolution of the waves using both the “G” and “H” codes. The G code is run with geodesic slicing, and the H code with harmonic slicing. We first look at runs with even parity waves having an amplitude of 10^{-5} and azimuthal mode number $m = 0$. Here the amplitude is the amplitude given by the Eppley packet [14] which corresponds to a perturbation in the metric function g_{xx} of about 0.025%. For such low amplitude waves,

the difference coming from nonlinearities in the Einstein equations is negligible. Initially the wave is at the coordinate center and expands outward as time increases. Fig. 9a plots g_{xx} at various times obtained by the “G” code and in Fig. 9b we blow up the region near the axis to show the wave in the metric function that rapidly falls off.

By $t = 5$, g_{xx} evolves to become nearly unity everywhere. Comparing the profile at $t = 5$ to the linearized solution in [15], we find that the error in g_{xx} is about 1.4×10^{-6} . Fig. 9c shows the evolution with the “H” code. We see that the results of the two codes are similar. The error in the “H” code at $t = 5$ is about 1.1×10^{-7} . If we require that the error remains $< 10^{-6}$, at $t = 5$ we see that we need 40 points/ λ for the “G” code and 10 points/ λ for the “H”. The dispersive nature of the “H” code is probably biasing this result by allowing the waves to disperse out faster.

In Fig. 10 we plot the error, as defined by Eq. (29), in g_{xx} as a function of grid resolution at time $t = 1$. Again we observe a convergence rate with an exponent of nearly two. We have also compared other metric components and various components of the Riemann tensor, and they all showed results agreeing to high accuracy with the linear analytic solution.

Next we study a case of higher amplitude perturbations with $A = 10^{-4}$ and $g_{xx} - 1 \sim 10^{-3}$. The evolution using the “G” code with geodesic slicing, and resolution $\Delta x = \Delta y = \Delta z = 0.1$ is shown for late times in Fig. 11a. The feature to note is that g_{xx} develops a dip at the origin. To distinguish if the dipping is due to numerical or physical nonlinear effects coming from the increased amplitude, we ran the same initial data with the linear evolution equation option of the code. The result is shown in Fig. 11b. No dipping is present whatsoever. This confirms that it *is* a nonlinear effect. As we pointed out earlier, there can be three types of non-linear effects: (i) numerical errors coupled with nonlinearity, (ii) coordinate effects due to nonlinearity, or (iii) nonlinear physics. We expect all three types to be present in the evolution. The question is, which one is most responsible for producing this dipping feature.

One might be tempted to identify this dip with the same spurious drifting coming from the coupling of the finite differencing error and the nonlinear term discussed in the previous section, namely effect (i). Both the drift in the previous section and the dip here are secular

evolutions in the region where the wave has passed. However, there is a major difference. In this case, the dipping is not converging away with higher resolution. In Fig. 11c we show the same quantities now evolved with $\Delta x = \Delta y = \Delta z = 0.05$. The dipping becomes slightly worse with the resolution doubled. We have carried this out at even higher resolutions with runs up to $\Delta x = \Delta y = \Delta z = 0.025$. We conclude that the dipping is not due to finite differencing error.

At this point we want to investigate another possibility for the cause of the dipping, which is not included in (i)-(iii) mentioned above. We note that the initial data set that we have used satisfies the initial constraint equations to first order only. While we evolve the initial data with the full nonlinear evolution equation, is it possible that there may be spurious effects due to this contradiction that leads to the dipping? This is the subject of the next subsection.

B. Quadrupole waves satisfying the IVP

To generate a set of initial data which is similar to what is studied in the previous subsection, we take the linear data as the metric \hat{g}_{xx} in the conformal space in the York formalism [16]. As the linear data set is constructed to be time symmetric with $\hat{K}_{ij} = 0$, the initial momentum constraint equations are trivially satisfied and it is straightforward to solve the initial Hamiltonian constraint equation to determine the conformal factor Ψ needed for the physical space metric $g_{xx} = \Psi^4 \hat{g}_{xx}$. For the case where the amplitude is taken to be 10^{-4} (the \hat{g}_{xx} of which is given in Fig. 11) the conformal factor is shown in Fig. 12a. We note that Ψ differs only slightly from 1, so that the initial data obtained through this procedure describes basically the same spacetime as studied in the previous subsection, except that now the initial data satisfy the constraint equation in full, and can be regarded as representing a physical spacetime as described by the Einstein equations up to the finite differencing approximation.

The evolution of this initial data is shown in Fig. 12b again using the G code with

geodesic slicing, and $\Delta x = \Delta y = \Delta z = 0.05$. We see that the time development is basically the same as in that of Fig. 11a. In particular, the dipping at the origin at late times is not affected.

After verifying that the dipping is not due to numerical truncation error (the effect doesn't decrease with resolution), and that it is independent of whether the IVP is solved or not, there are two possibilities left. The dipping is either due to (ii) nonlinear coordinate effects, or (iii) nonlinear physics, as discussed and labeled in the introduction section. To distinguish which one is the main cause, we look at variables that are representative of the actual geometry. We studied various components of the four dimensional Riemann tensor, e.g., $\mathfrak{R}_{\alpha\beta\gamma\delta}$, the Riemann invariants I and J [20], and the pseudo energy-momentum tensor [22]

$$\tau_{\mu\nu} = \frac{1}{8\pi G} \left(\mathfrak{R}_{\mu\nu} - \frac{1}{2} g_{\mu\nu} \mathfrak{R} - \mathfrak{R}_{\mu\nu}^{(1)} + \frac{1}{2} \eta_{\mu\nu} \mathfrak{R}^{(1)} \right), \quad (44)$$

where $\mathfrak{R}_{\mu\nu}^{(1)}$ is the part of the four dimensional Ricci tensor that is linear in the deviation of the metric from flat spacetime. For simplicity, we assume $\mathfrak{R}_{\mu\nu} = 0$ when evaluating Eq. (44) numerically. We note that this $\tau_{\mu\nu}$ is meaningless if the initial data satisfy the constraints only to the linear order. For this reason $\tau_{\mu\nu}$ is not used in the analysis of any of the linearized initial data in the previous section.

In Figs. 13a-g we compare the “G” code geodesic slicing evolution to the maximal slicing case. Notice that (1) even while the metric is dipping in the geodesic slicing case all the components of the Riemann tensor studied, the Riemann invariants, and τ_{tt} , all remain small, and are consistent with returning to zero at late times (see Figs.13b and 13c). (2) In the maximal slicing case, there is no dipping of metric components (Fig.13d). (3) There is good agreement in the Riemann tensor components, the Riemann invariants, and τ_{tt} between the geodesic and the maximal slicing cases (Figs. 13e and 13f), although the metric functions behave differently. In Fig. 13g, we show the evolution of lapse in the maximal slicing case. We see that the lapse is very close to one throughout the spacetime. This means that in terms of proper time evolved, the geodesic slicing case and the maximal slicing case are not

that different.

This strongly suggests that the dipping should be attributed to nonlinear coordinate effects. The energy of the wave initially sitting at the origin sets the coordinate lines (which move normal to the slicing in the case of zero shift) into free fall towards the origin. As the wave moves outward, the geometry near the origin returns to being flat. However, with geodesic slicing and no shift vector, there is nothing to stop the motion of coordinate lines. They keep drifting towards the center where the wave was, causing the metric functions to dip there. With maximal slicing, the motion of the coordinate lines is changed as the normal of the constant time surface changes with respect to the four geometry. This is enough to stop the secular motion of the coordinate lines in this weak field case without having the lapse collapse in any significant manner. This kind of gauge problem in evolving with geodesic slicing is well noted in the literature [23]). From Eq. (3) we can compute the evolution of K for geodesic slicing, which, using the hamiltonian constraint reduces to:

$$\partial_t K = K_{mn} K^{mn} . \quad (45)$$

The RHS of this equation is always non-negative. Therefore, the convergence K of the geodesics tends to increase without limit, resulting in a coordinate singularity on a free-fall time scale. See Ref. [23] for a full discussion. Here we found that the dipping seen in Fig. 13a is due solely to this effect.

By comparing the metric functions obtained from a linear evolution to a nonlinear evolution, we can define a qualitative measure of the time at which nonlinear coordinate effects become present. We do this by defining $t_{critical}$ as the time when the RMS relative difference of the linear and nonlinear evolutions disagree by 10%. Since this RMS value is a global measure, we expect our results to depend on the specific energy distribution of the wave model that we are evolving. In Fig. 14a we compare the critical time as a function of the size of the initial metric function perturbation. We see that the critical times scales roughly as a power law. The error bars in the graph come from the fact that the data is only analyzed in time intervals of $\Delta t = 0.1$.

To determine the time at which nonlinear geometric effects occur, we define a similar critical time, but now comparing the RMS relative difference of the linear and nonlinear evolutions of the curvature invariant I . Again, we define $t_{critical}$ as the time at which the two evolutions disagree by 10%. The results are shown in Fig. 14b, again plotted against the size of the initial metric function perturbation. The critical time for nonlinear geometric effects occurs at a later time than that of nonlinear coordinate effects for the amplitudes considered here.

VII. CONCLUSION

In this first paper in the series, we studied various aspects of our 3D codes in evolving gravitational waves. We show how the accuracy of the evolution can be analyzed through various monitors built into the codes. This includes violation of the hamiltonian constraint, Fourier spectrum analysis, as well as convergence tests. These studies are not only crucial for our using these codes in the future, but are also useful for other groups who may want to build similar 3D codes.

We focused on the difficulties in evolving low to moderate amplitude gravitational waves. They have amplitudes low enough so that one has a good physical understanding of the physics involved, but at the same time large enough to enable non-linear effects to emerge. We studied (i) the coupling between numerical errors and nonlinearity, and (ii) coordinate effects due to nonlinearity, with specific examples. We discussed the strategies used in identifying the cause of the non-linear effects. In this process we emphasize the importance of the flexibility of being able to use different numerical schemes, different choice of coordinate conditions, different formulations of the Einstein equations (G and H formulations), and different equations (linear vs. nonlinear equations). This flexibility, and the availability of many “monitoring devices” in the codes, such as the scalar Riemann invariants, pseudo energy-momentum tensor, and hamiltonian constraint, have been crucial in our understanding of the nonlinear effects.

With these in hand, we are now proceeding to study the collision of 3D wave packets (packets finite in size in all three spatial dimensions). We consider this to be possibly just next in importance in geometrodynamics to the collision of two black holes. The results will be reported in later papers in the series.

ACKNOWLEDGMENTS

We thank Steve Brandt for coding up the Riemann invariant routines used in this paper. This work was supported by NSF grants PHY94-04788, 94-07882, and 96-00587. The calculations were performed at NCSA on the Thinking Machines CM-5 and at the Pittsburgh Supercomputing Center on the Cray C-90. WMS would like to thank the support of the Institute of Mathematical Sciences of the Chinese University of Hong Kong. In the late stage of the preparation of this paper, a paper by Shibata and Nakamura appeared (Ref. [24]) reporting on their numerical study of gravitational waves based on a code they developed independently.

REFERENCES

- [1] K. Khan and R. Penrose, *Nature* **229**, 185 (1971).
- [2] F. Tipler, *Phys. Rev. D* **22**, 2929 (1980).
- [3] R. Matzner and F. Tipler, *Phys. Rev. D* **29**, 1575 (1984).
- [4] U. Yurtsever, *Phys. Rev. D* **37**, 2790 (1988).
- [5] U. Yurtsever, *Phys. Rev. D* **38**, 1731 (1988).
- [6] A. Abrahams and C. Evans, *Phys. Rev. D* **46**, R4117 (1992).
- [7] A. Abrahams and C. Evans, *Phys. Rev. Lett.* **70**, 2980 (1993).
- [8] R. Vogt, in *Sixth Marcel Grossman Meeting on General Relativity (Proceedings, Kyoto, Japan, 1991)*, edited by H. Sato and T. Nakamura (World Scientific, Singapore, 1992), pp. 244–266.
- [9] W. W. Johnson and S. M. Merkowitz, *Phys. Rev. Letter* **70**, 2367 (1993).
- [10] P. Anninos *et al.*, *Phys. Rev. D* **52**, 2059 (1995).
- [11] R. Arnowitt, S. Deser, and C. W. Misner, in *Gravitation: An Introduction to Current Research*, edited by L. Witten (John Wiley, New York, 1962).
- [12] C. Bona and J. Massó, *Phys. Rev. D* **40**, 1022 (1989).
- [13] C. Bona and J. Massó, *Phys. Rev. Lett.* **68**, 1097 (1992).
- [14] K. Eppley, in *Sources of Gravitational Radiation*, edited by L. Smarr (Cambridge University Press, Cambridge, England, 1979), p. 275.
- [15] S. Teukolsky, *Phys. Rev. D* **26**, 745 (1982).
- [16] J. York, in *Sources of Gravitational Radiation*, edited by L. Smarr (Cambridge University Press, Cambridge, England, 1979).

- [17] C. W. Misner, K. S. Thorne, and J. A. Wheeler, *Gravitation* (W. H. Freeman, San Francisco, 1973).
- [18] D. Bernstein, D. Hobill, and L. Smarr, in *Frontiers in Numerical Relativity*, edited by C. Evans, L. Finn, and D. Hobill (Cambridge University Press, Cambridge, England, 1989), pp. 57–73.
- [19] C. Bona, J. Massó, E. Seidel, and J. Stela, Phys. Rev. Lett. **75**, 600 (1995).
- [20] M. M. D. Kramer, H. Stephani and E. Herlt, *Exact Solutions of Einstein's Field Equations* (Cambridge University Press, Cambridge, 1980).
- [21] C. Evans, in *Dynamical Spacetimes and Numerical Relativity*, edited by J. Centrella (Cambridge University Press, Cambridge, England, 1986), pp. 3–39.
- [22] S. Weinberg, *Gravitation and Cosmology: Principles and Applications of the General Theory of Relativity* (John Wiley and Sons, New York, 1972).
- [23] L. Smarr and J. York, Phys. Rev. D **17**, 2529 (1978).
- [24] M. Shibata and T. Nakamura, Phys. Rev. D **52**, 5428 (1995).

FIGURES

FIG. 1. The evolution of the metric function g_{xx} is shown for a plane wave with shape parameters $\sigma = 2.0$, $\lambda = 1.0$, $A_L = 0.00001$, $A_R = 0$, and $a = 3$. The wave is shown at times; $t=0$, $t=3$, and $t=6$. This wave was evolved with 40 points per wavelength

FIG. 2. The evolution of the metric function g_{xx} is shown for a plane wave with shape parameters $\sigma = 2.0$, $\lambda = 1.0$, $A_L = 0.00001$, A_R , and $a = 0$. Periodic boundary conditions are applied to allow the wave to evolve for a long time. The evolutions (a)-(c) are done with the H code, and the evolutions (d)-(f) are done with the G code. Here we see the effects of dispersion when insufficient resolution is used.

FIG. 3. The log of the RMS error is plotted against the log of the resolution Δx , to test the convergence of the code. Here the error E is defined in the text with respect to the linear solution. Although we are evolving the solution with the full non-linear equations, with the small amplitudes used, we expect the wave to behave linearly. Second order methods were applied throughout, so we expect the slope of this graph, m , to be 2.

FIG. 4. The real part of the Fourier transform of the metric functions plotted in Fig. 2b, and Fig. 2e are shown to compare the effects of dispersion and dissipation. The H code is found to be more dissipative and dispersive than the G code.

FIG. 5. The curvature invariant I is plotted for plane wave evolutions. It is known that all curvature invariants are zero for plane wave spacetimes, and in this figure we see I converging to zero as we increase the resolution.

FIG. 6. The metric function g_{xx} is shown for two plane waves with the same parameters as the single wave packet, except a larger amplitude $A_L = A_R = 0.025$, and centered at $z = \pm 3$. In (a) we show the evolution with the G code, and a fully nonlinear evolution. Note the drifting that takes place in the region where the waves collide. In (b) we show the same initial data now evolved with the linear evolution equations. No drifting is present when the linear evolution equations are used. In (c) we show the same initial data evolved with the full nonlinear evolution but now with a MacCormack-like finite differencing scheme. The drifting is now greatly reduced. In (d) we evolve the initial data with the H code, and the drifting is similar to that found in (c). In (e) we again use the nonlinear G code, but now with higher resolution compared to (a). We find that the drifting decreases with resolution. In general we find the drifting is a nonlinear effect, that depends on the resolution and finite-differencing scheme used.

FIG. 7. A scalar field f , evolved with a nonlinear wave equation with nonlinear terms similar to those found in the Einstein equations is shown. The shape of the wave packets is similar to those used in the collision of two waves in the previous section. A staggered leapfrog scheme is used. In (b) we show a blow up of the region of interaction to show the drifting.

FIG. 8. The quantity $e^{-f} - 1$ is shown plotted against time for both the leapfrog and MacCormack-like schemes. This shows a solution of the form $f(t) = -\ln(c_1 t + c_2)$ being excited by numerical error. The constants c_1 and c_2 are measured from the graph and depend on the resolution and numerical scheme used. The MacCormack scheme has a much smaller drift rate with $c_1 = 1.4 \times 10^{-7}$ and $c_2 = 1.0$, as compared to the leapfrog scheme with $c_1 = -9.8 \times 10^{-5}$ and $c_2 = 1.0$. These results were obtained with $\Delta x = 0.05$. We see that with both these methods this solution converges away with increased resolution.

FIG. 9. The metric function g_{xx} is shown for a small amplitude Teukolsky wave with azimuthal mode number $m = 0$. This corresponds to a perturbation in the metric function of about 0.025%. In (a) we show the evolution using the G code. In (b) we magnify the region near the axis showing the wave in the metric function which rapidly drops off as the wave travels outward. In (c) we show the evolution with the H code.

FIG. 10. The log of the RMS error is again plotted as in Fig. 3, to test the convergence of the code. At $t = 1$ we get a convergence rate of 1.95 for the G code, and 1.91 for the H code.

FIG. 11. The metric function g_{xx} is shown for a moderate amplitude Teukolsky wave with azimuthal mode number $m = 0$. This corresponds to an initial perturbation in the metric function of about 0.5%. The early part of the evolution is virtually identical to Fig. 9a, but at late times, after the wave has dispersed out, we now see a dipping in the metric function near the origin. In (a) the initial data is evolved with the full nonlinear equations using the G code, and we clearly see the late time dipping. In (b) we evolve with the linear evolution equations and see no evidence of the dipping. In (c) we again use the nonlinear evolution, but increase the resolution and find the dipping does not converge away.

FIG. 12. In (a) we show the conformal factor after using the Teukolsky initial data and solving the IVP. In (b) we show the evolution of this initial data which now solves the constraint equation up to numerical error. We see that the evolution of this data is virtually the same as in Fig. 11a and the dipping of the metric function is still present.

FIG. 13. The effect of slicing on the evolution of the quadrupole wave + IVP initial data. In (a) we see the evolution of the metric function g_{xx} with geodesic slicing. In (b) we show τ_{tt} , the stress-energy pseudo-tensor. In (c) we show the curvature invariant I . In (d) we show the same initial data now evolved with maximal slicing. Note that there is no dipping in the metric function. In (e) we again show τ_{tt} , and in (f) the curvature invariant I . Note that even though the evolution of the metric function differs with slicing, τ_{tt} and I remain the same which suggests that we are seeing a coordinate, rather than geometric, effect. In (g) we show the lapse α . Note that α is very close to one. It is the shape of the lapse rather than its size, that keeps the metric function from dipping near the origin. We also note that the pseudo-tensor and the invariants are not defined in the first boundary cells in our computational domain, and so we arbitrarily assign a value of zero to the left-most point in the graphs.

FIG. 14. We define a critical time $t_{critical}$ at which the RMS relative difference of the linear evolution disagrees with nonlinear evolution by 10%. In (a) we look at $t_{critical}$ for the metric function g_{xx} , and compare it against the size of initial perturbation in the metric function g_{zz} . Since the metrics show the coordinate dipping, this is a measure of the onset of nonlinear coordinate effects. We find that there is an approximate power law dependence of $t_{critical}$. The error bars in this graph come from the fact that the data is only analyzed in time intervals of $\Delta t = 0.1$. In (b) we do the same, but for the curvature invariant I . Since the invariant is coordinate independent, it is a measure of nonlinear geometric effects. We find that nonlinear geometric effects occur at a later time than nonlinear coordinate effects for the amplitudes considered here.

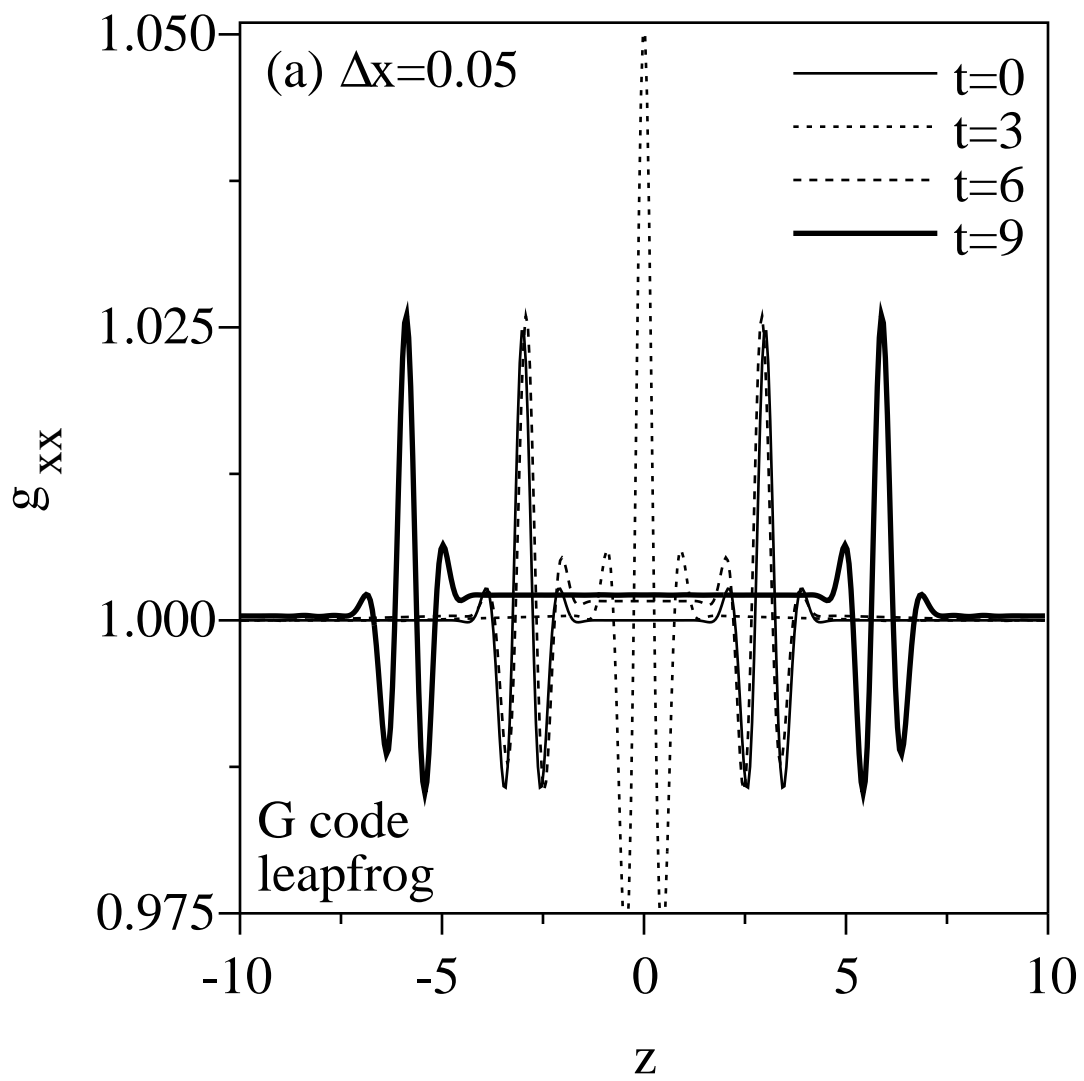


Fig. 6a

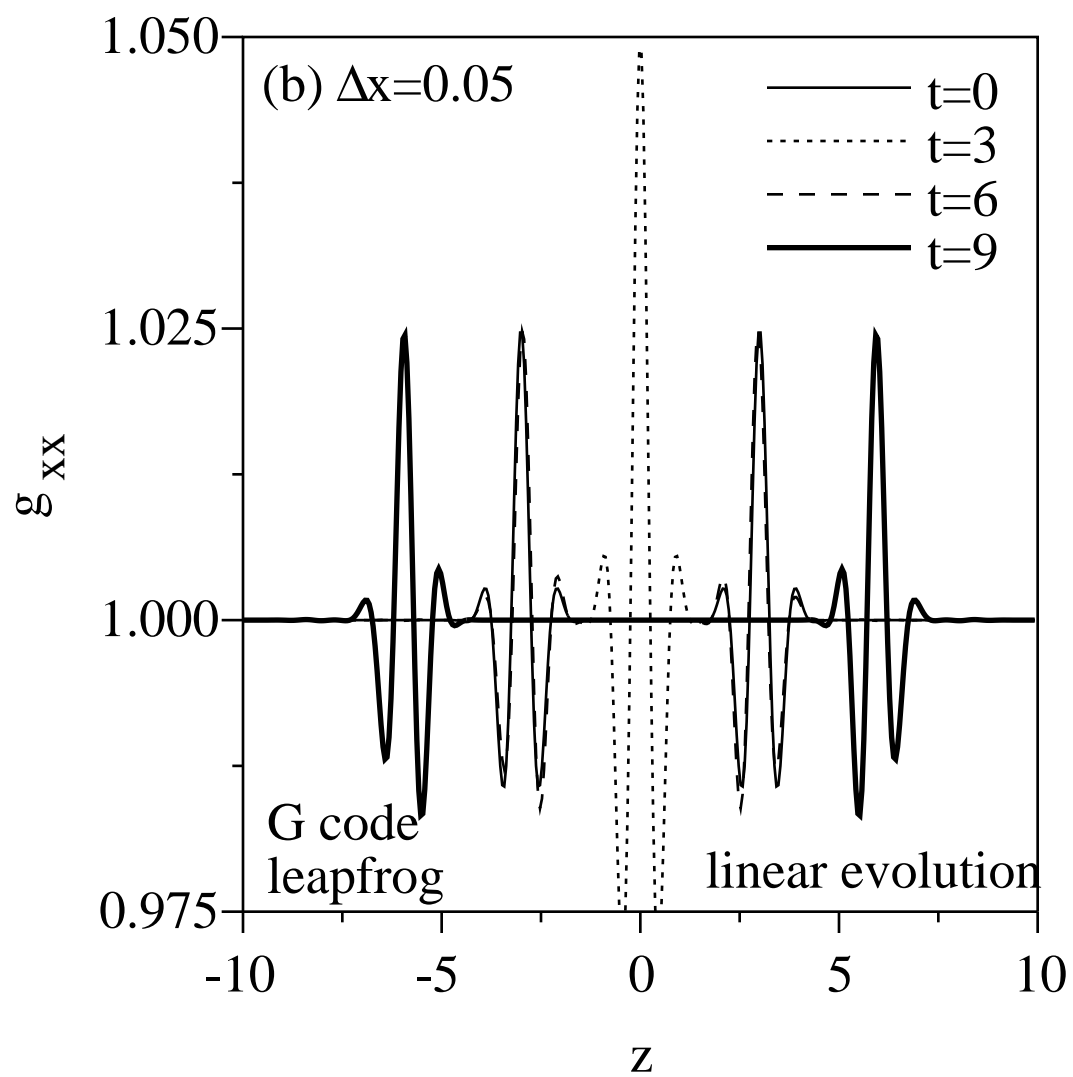


Fig. 6b

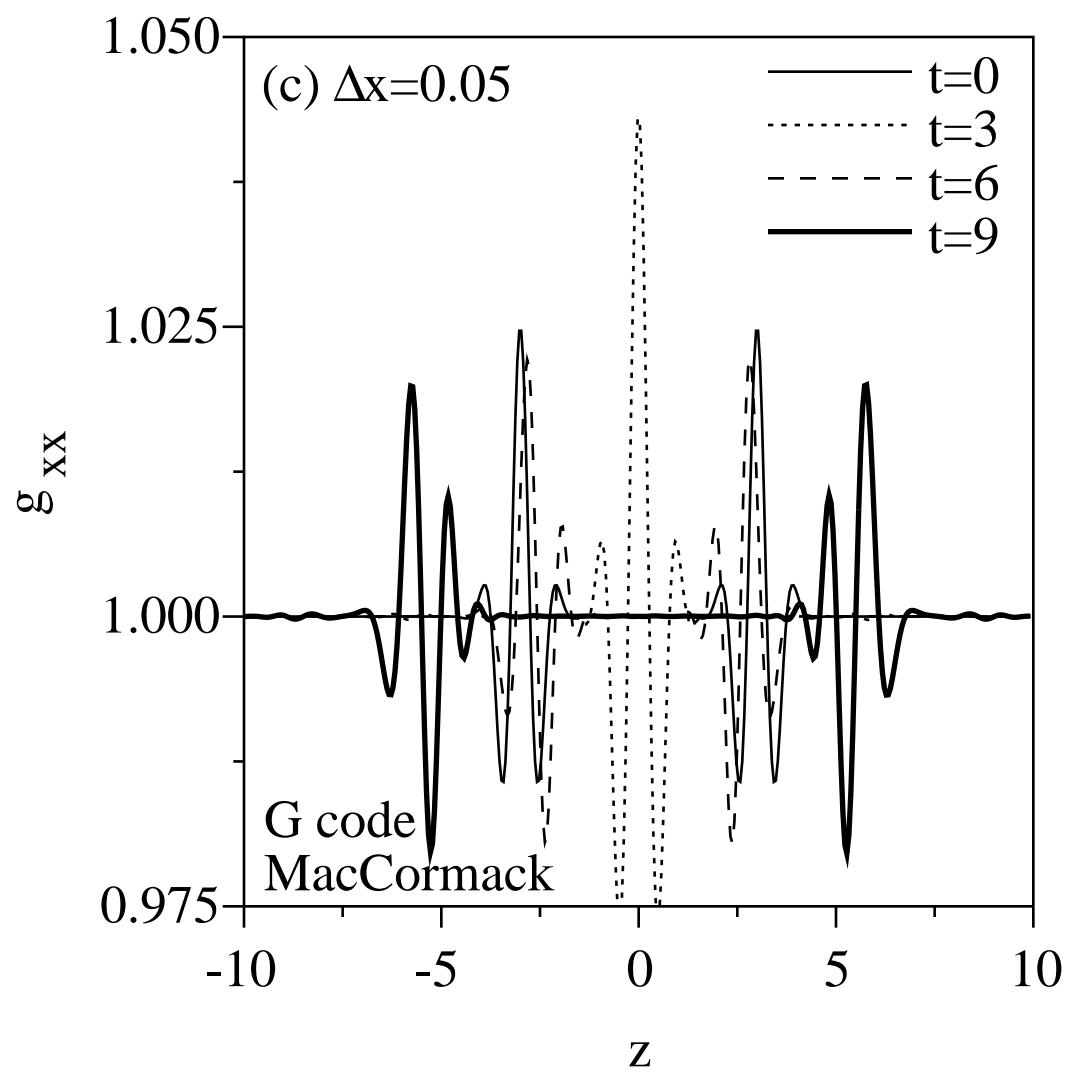


Fig. 6c

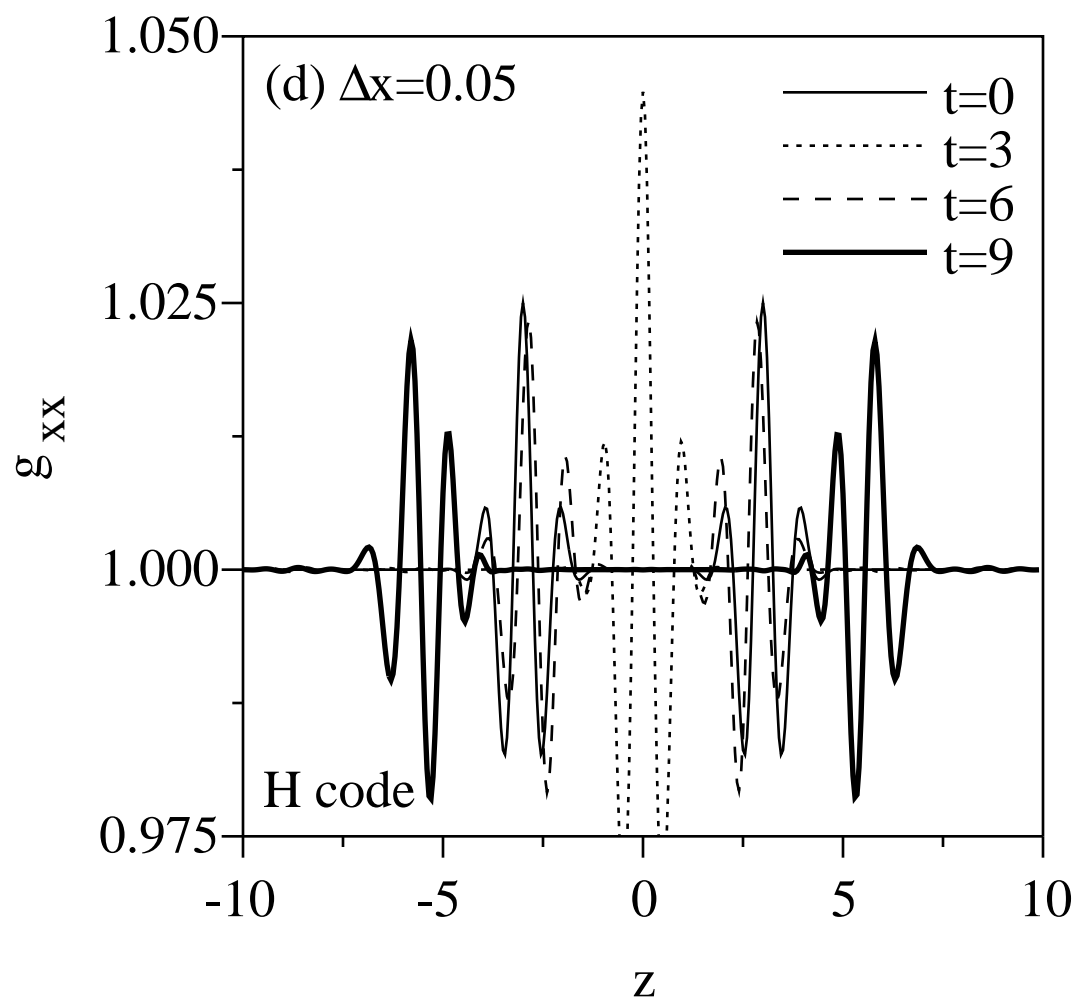


Fig. 6d

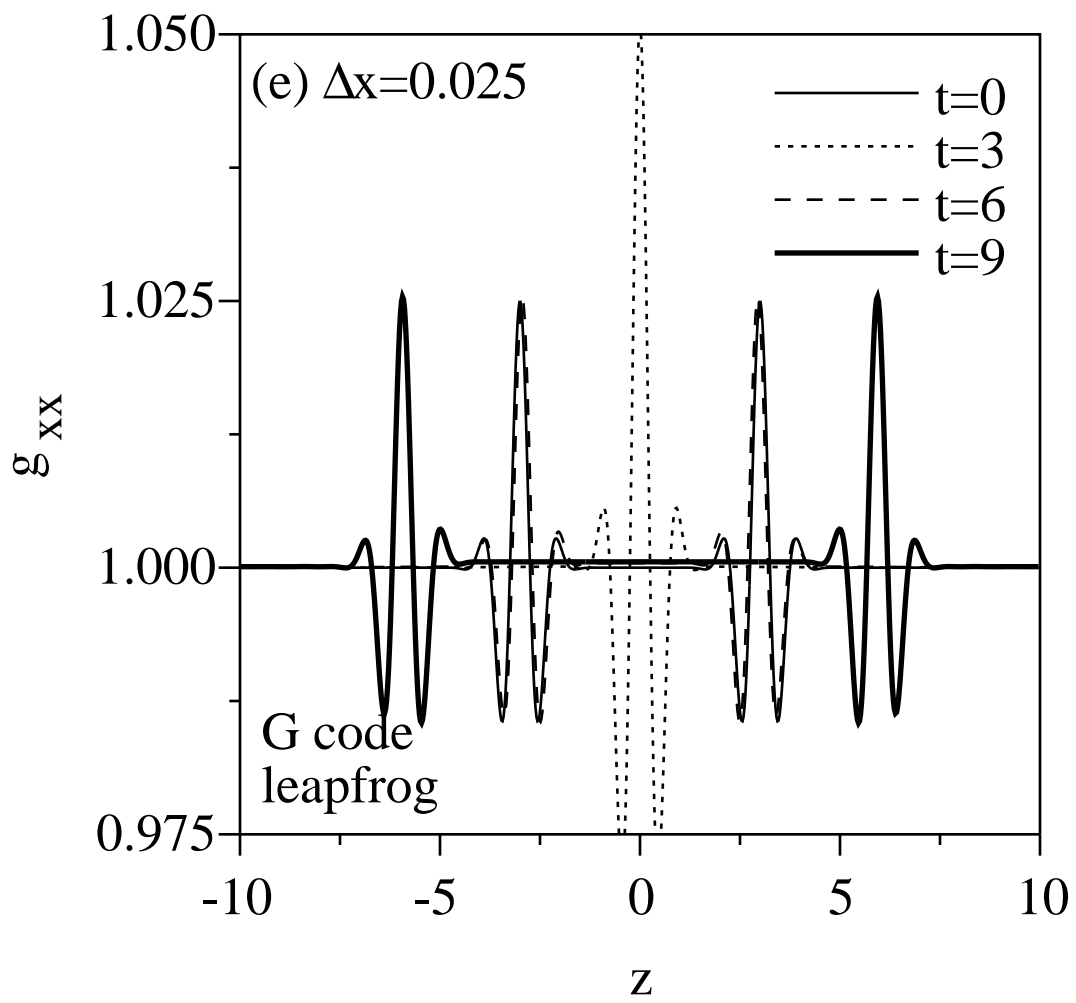


Fig. 6e

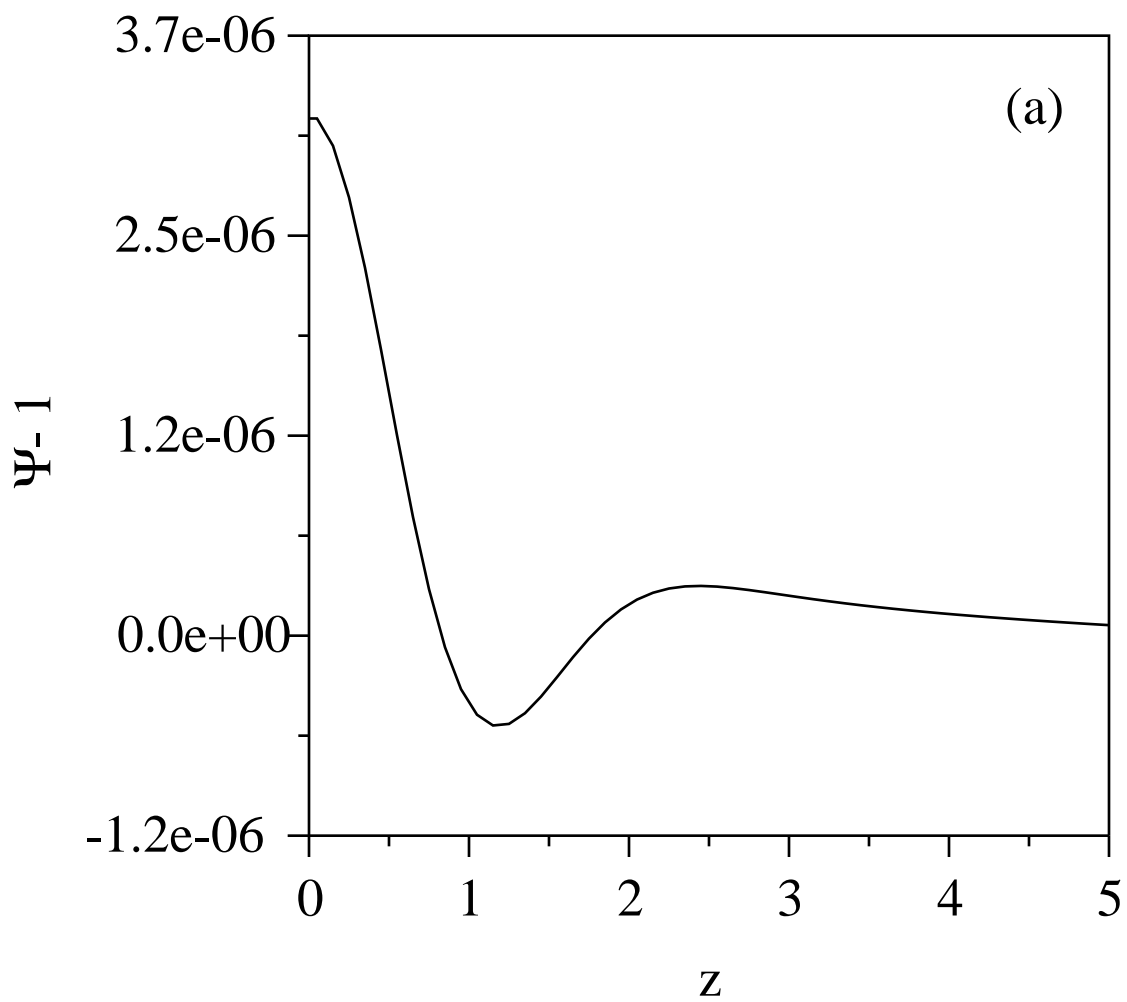


Fig. 12a

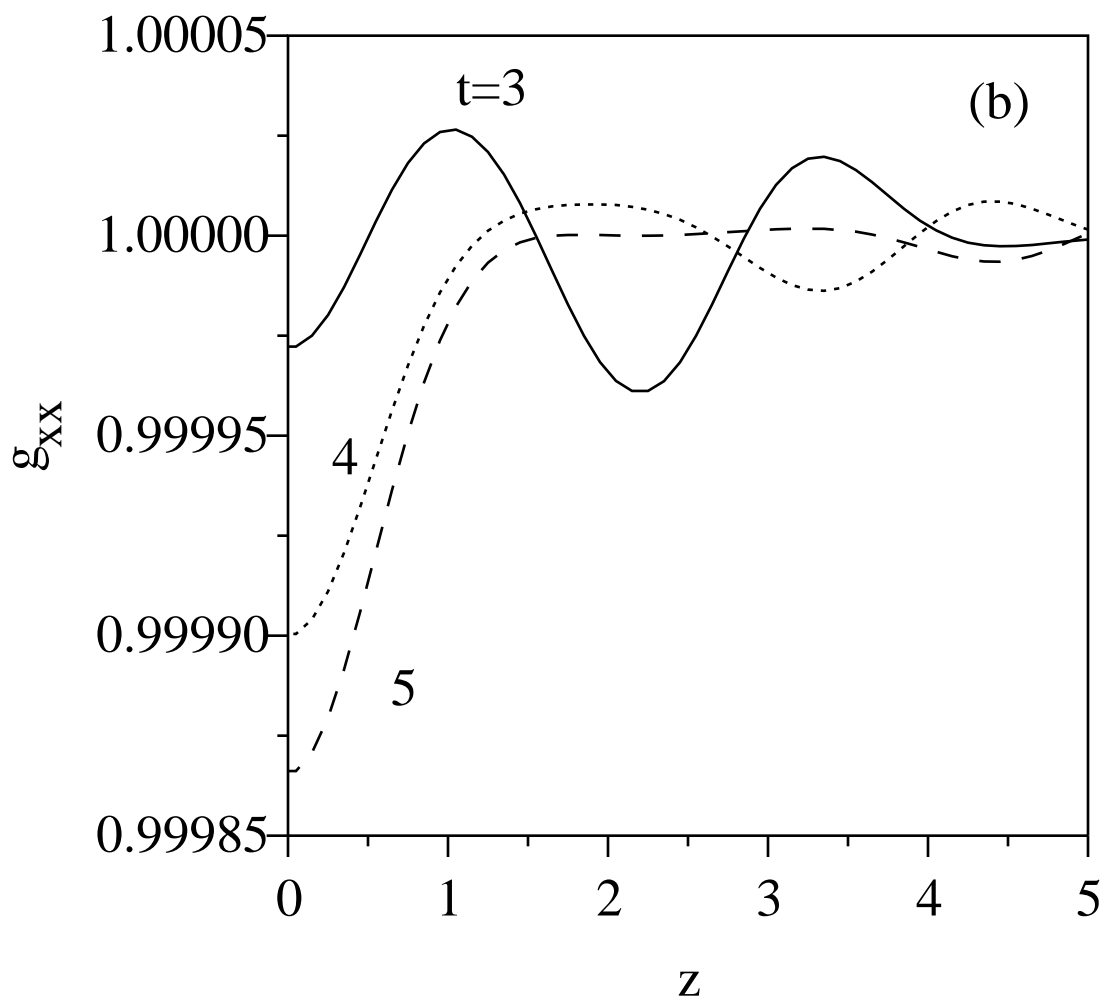


Fig. 12b

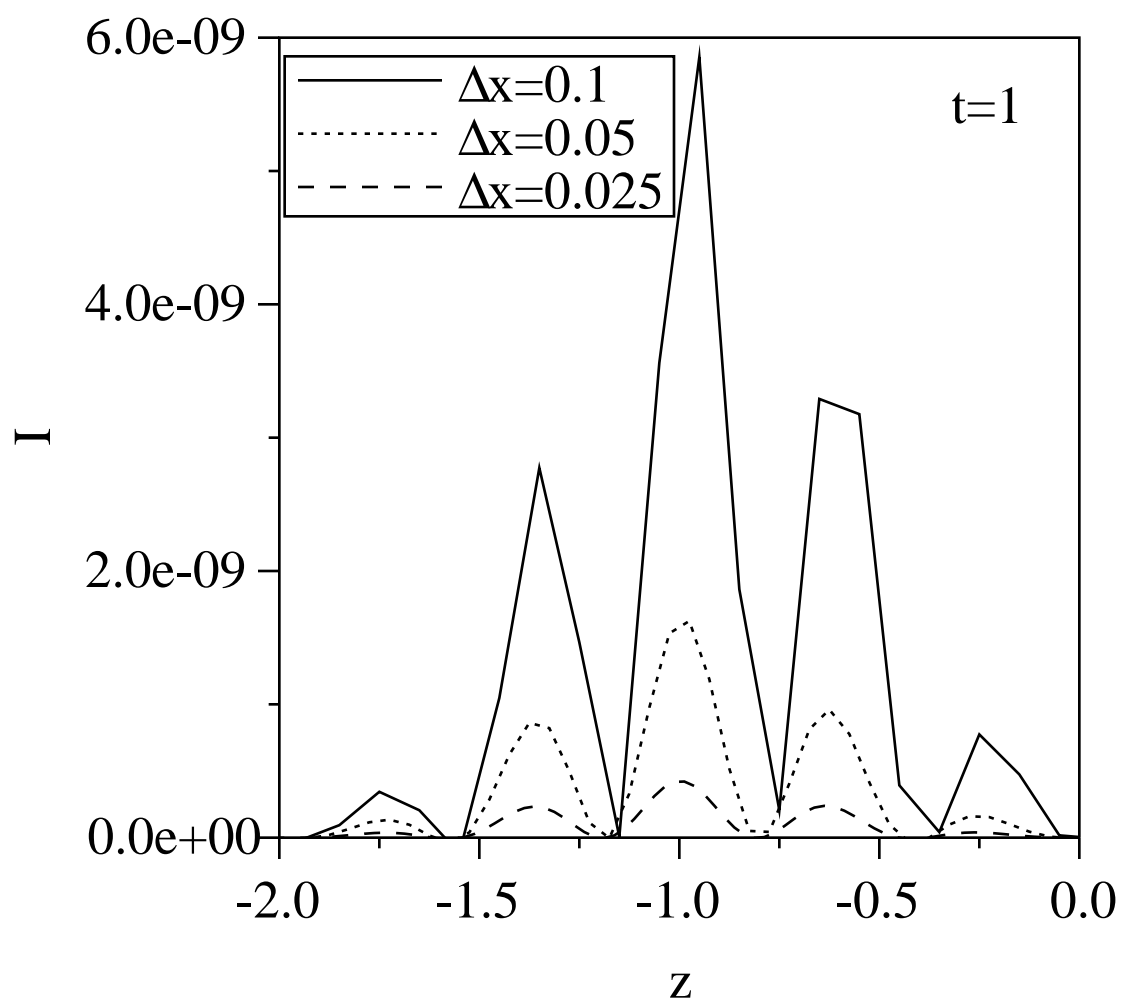


Fig. 5

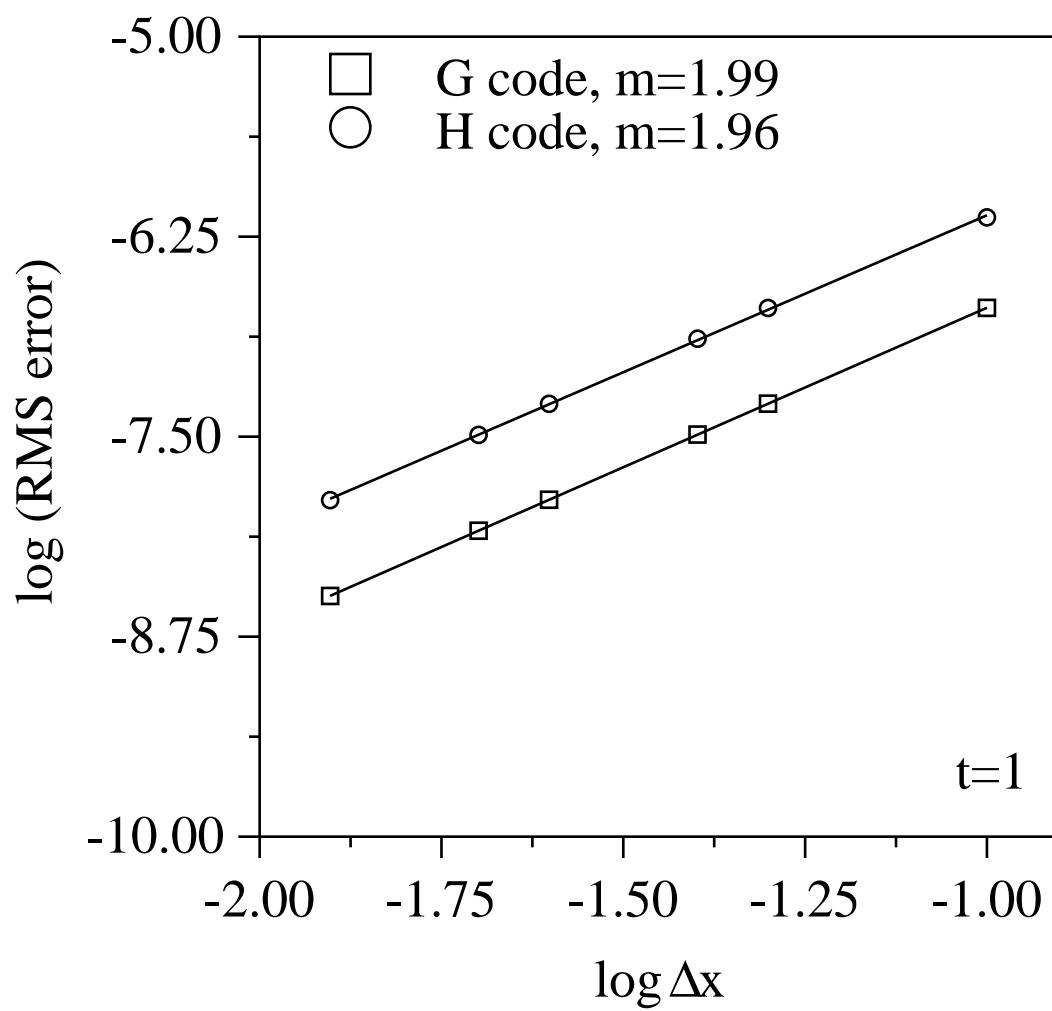


Fig. 3

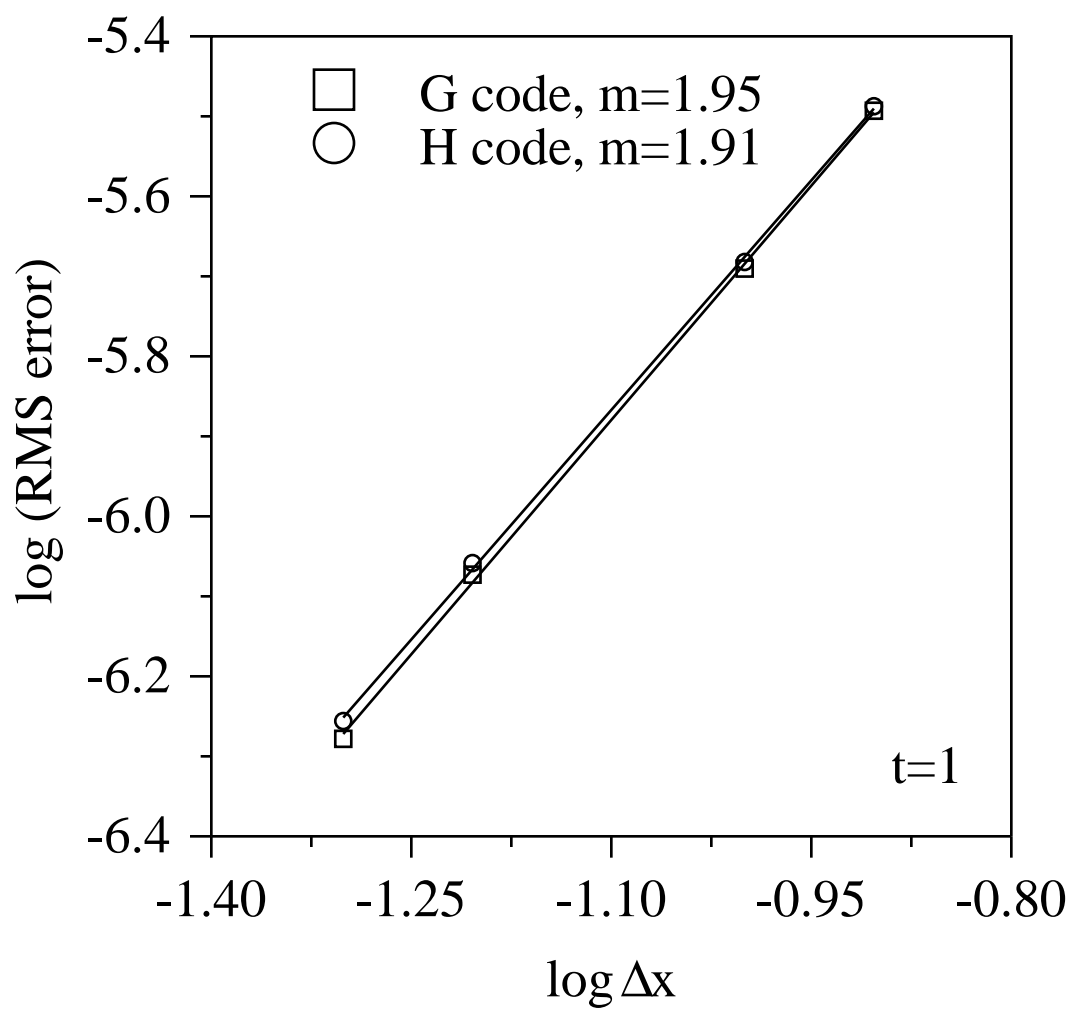


Fig. 10

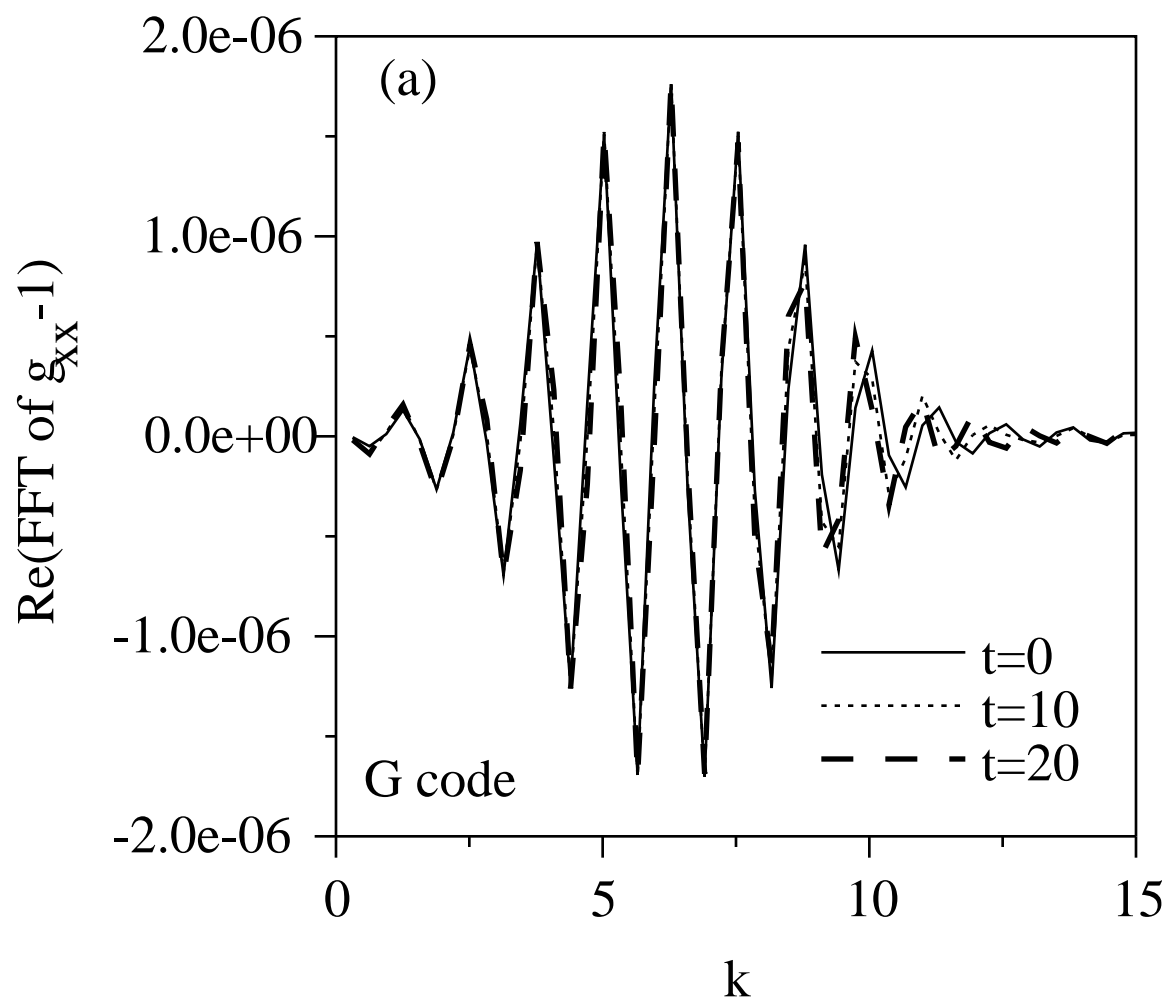


Fig. 4a

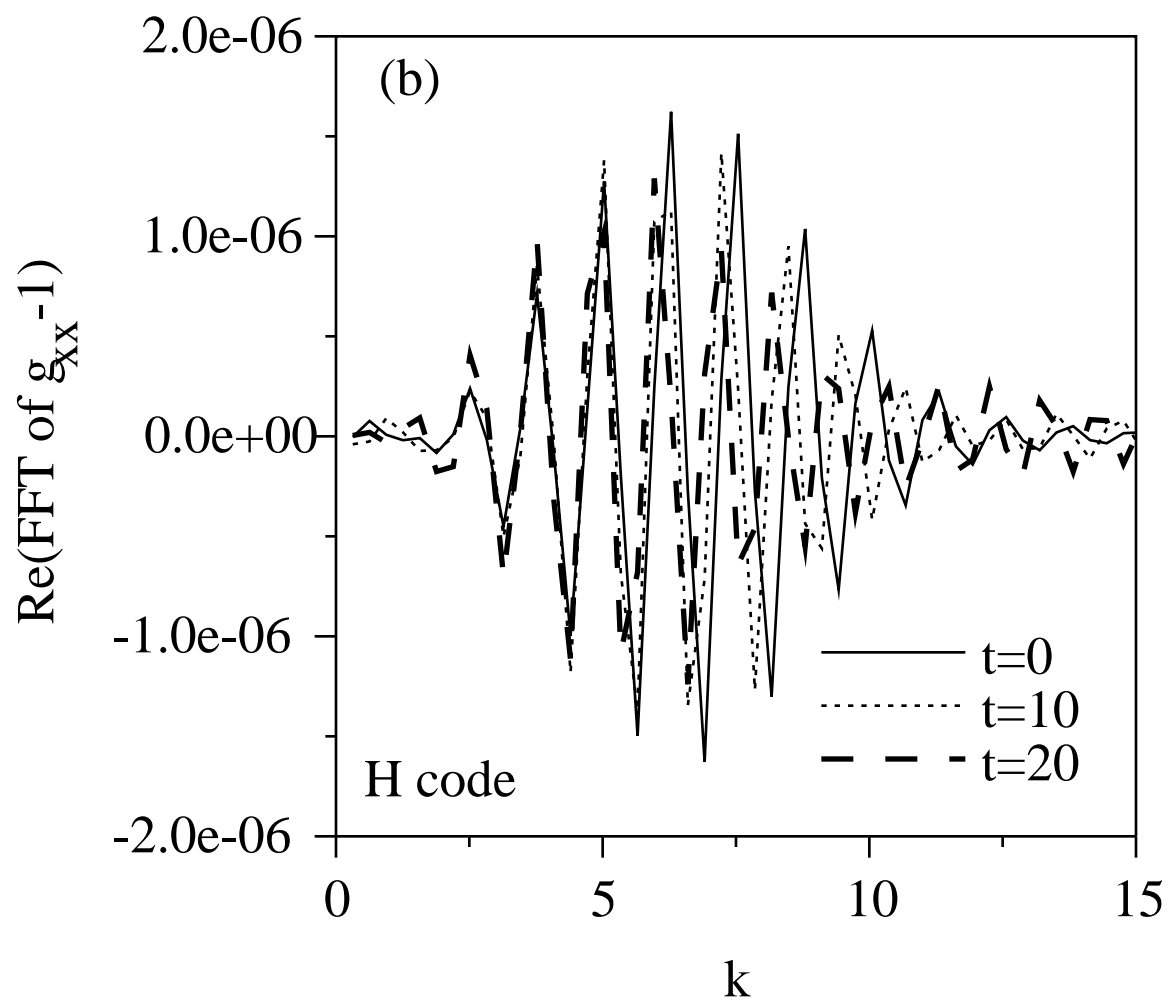


Fig. 4b

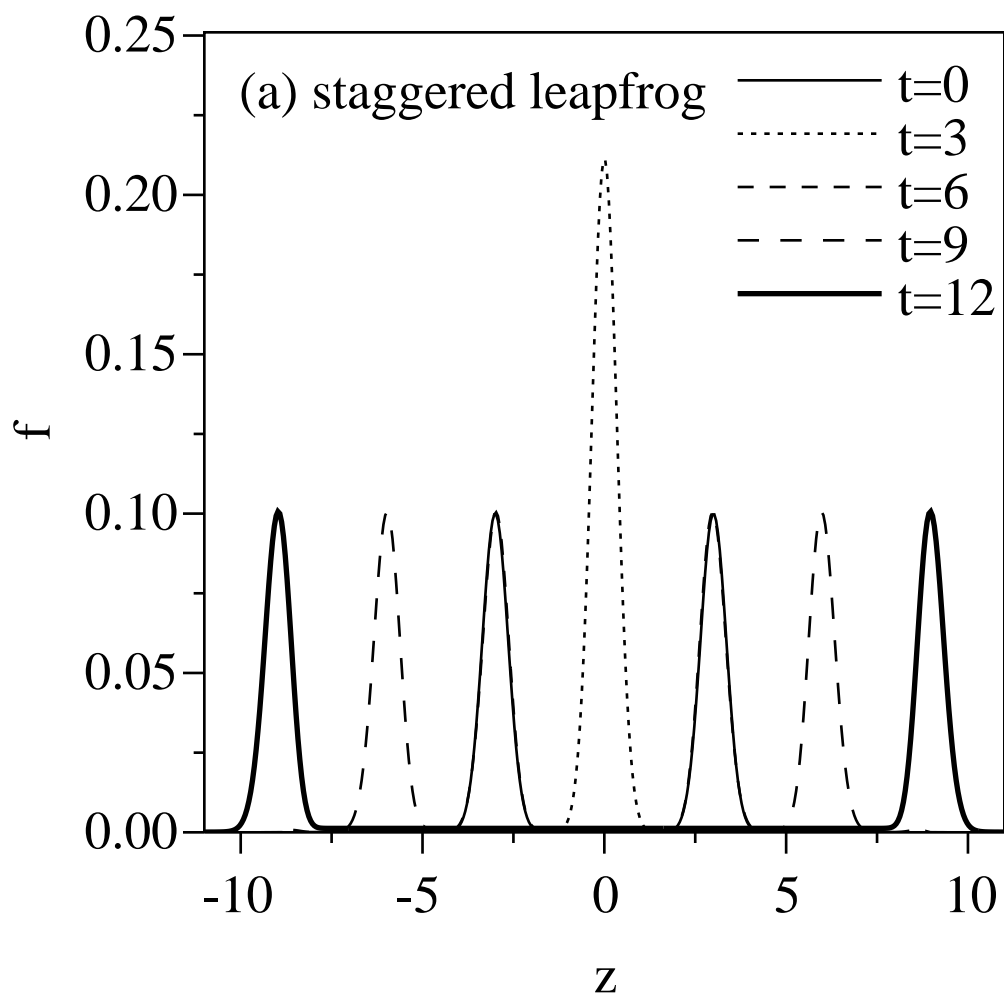


Fig. 7a

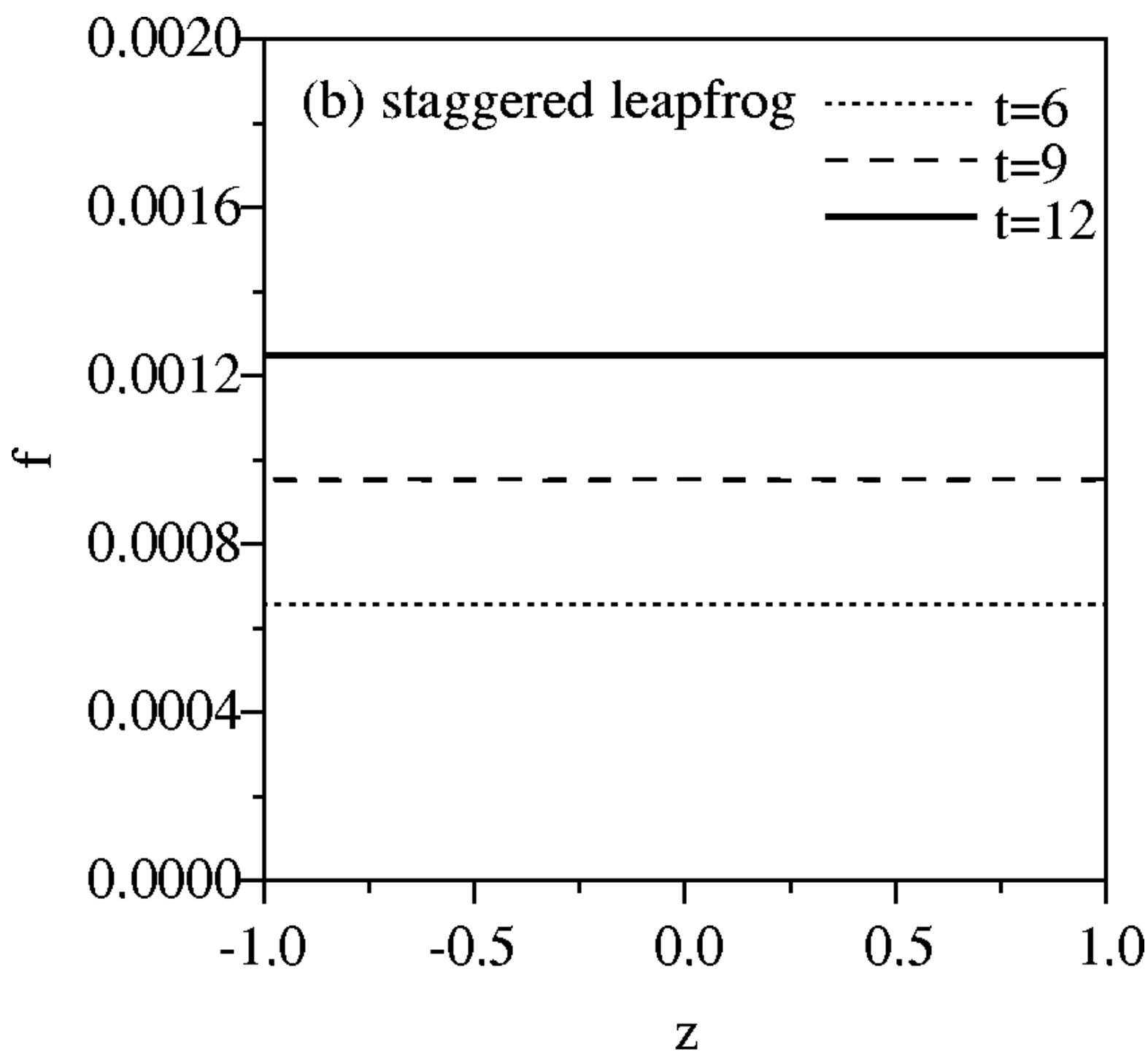


Fig. 7b

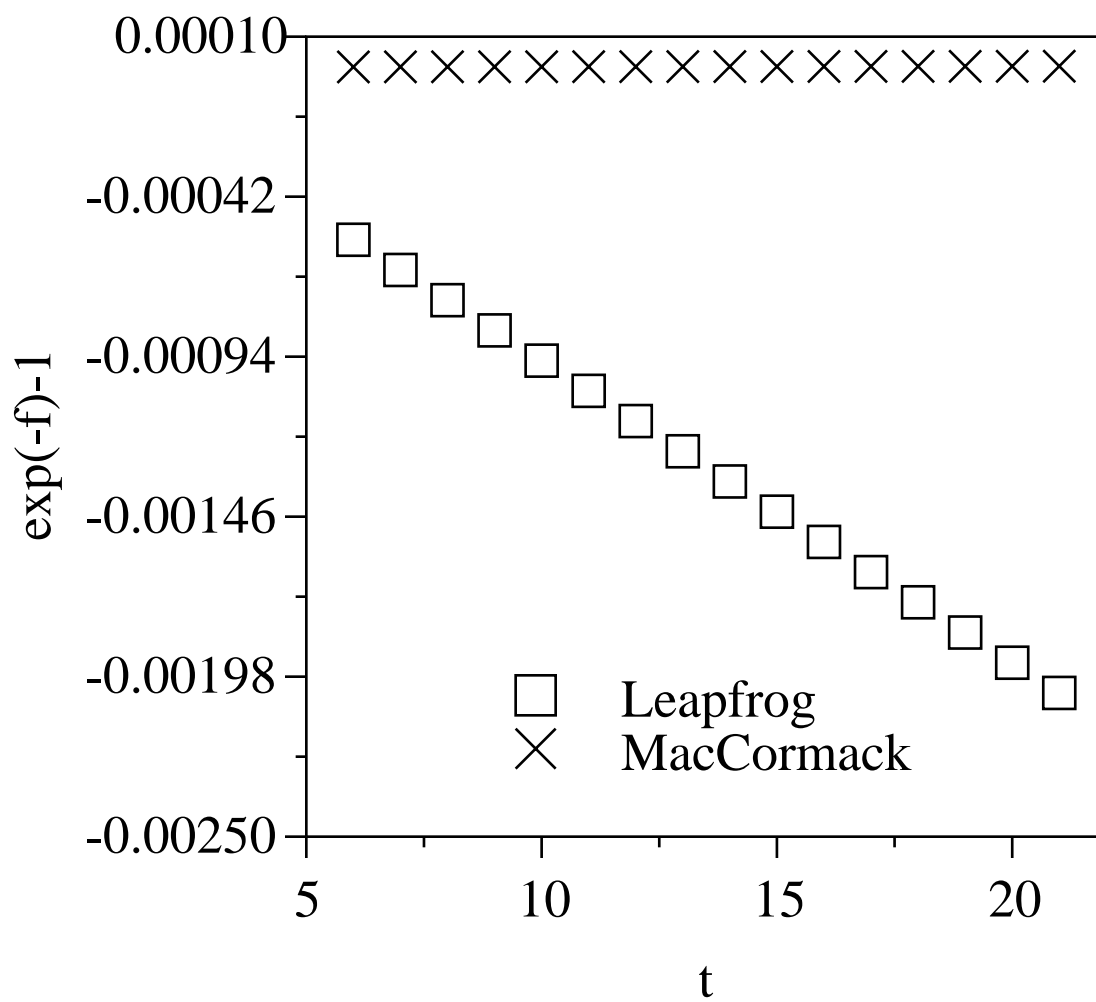


Fig. 8

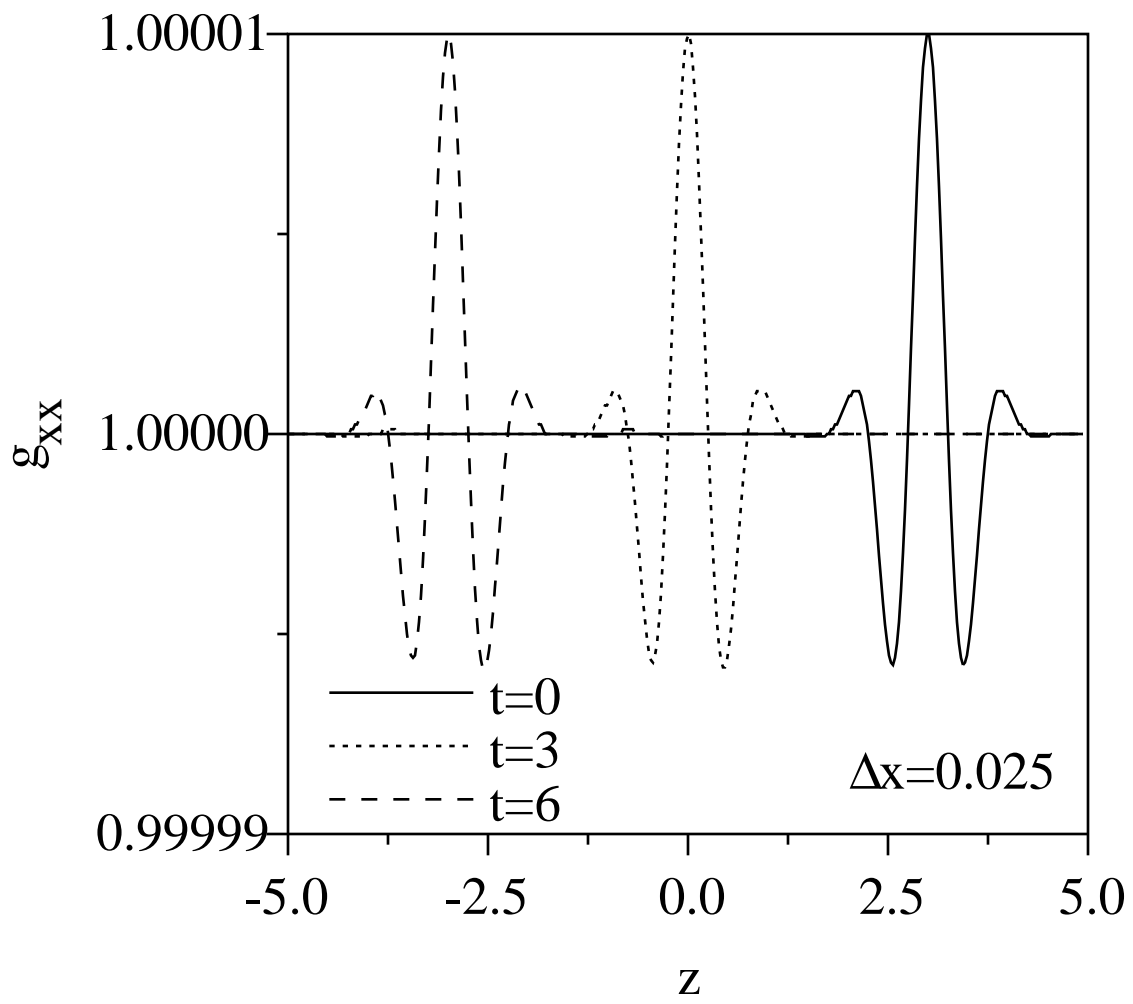


Fig. 1

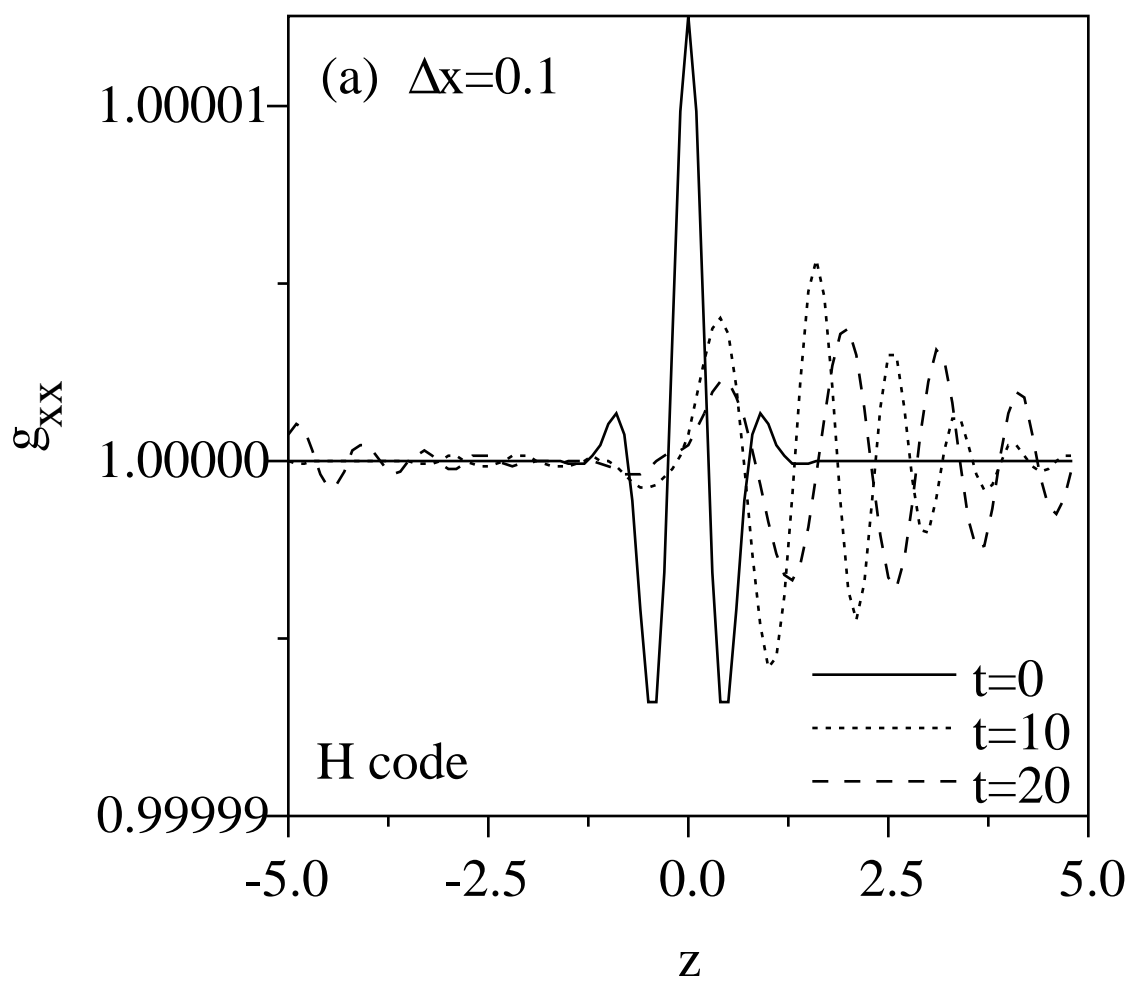


Fig. 2a

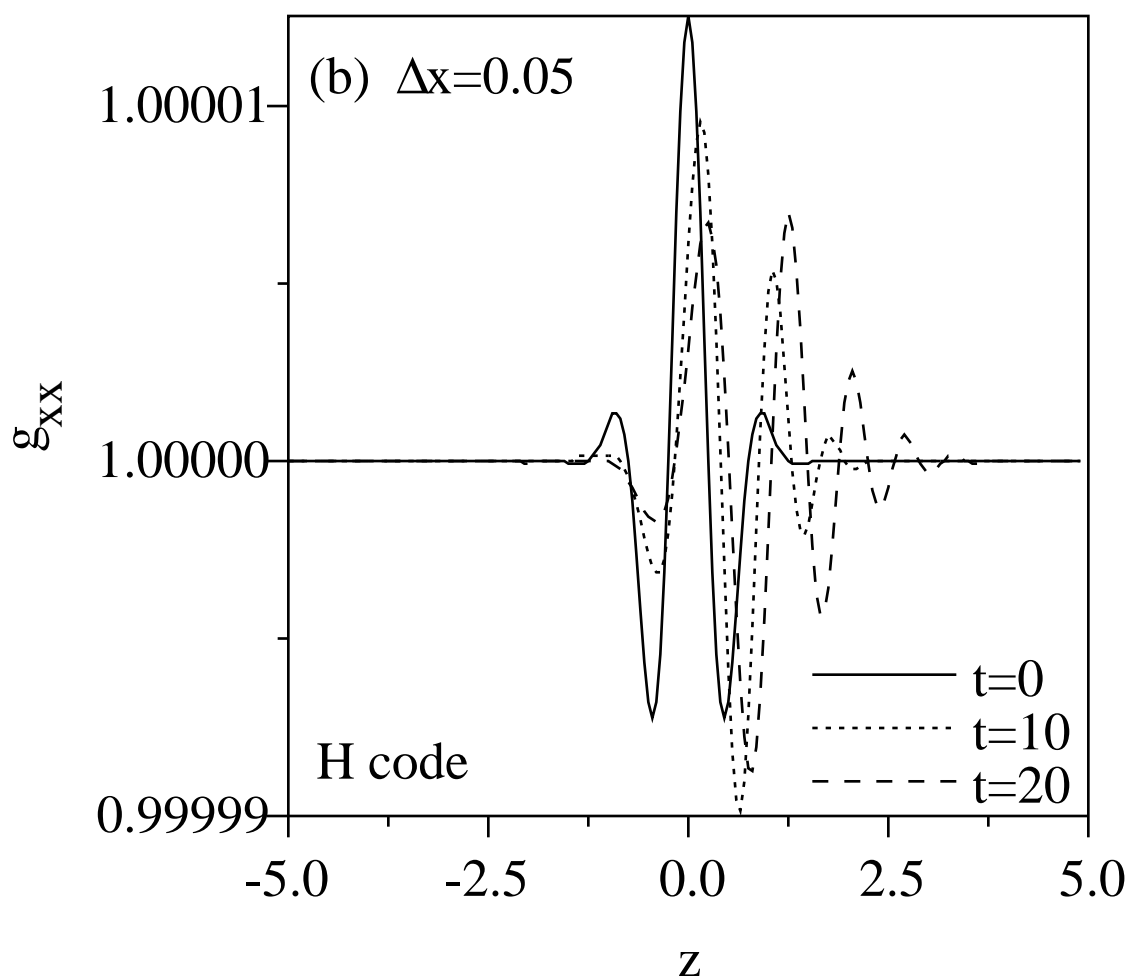


Fig. 2b

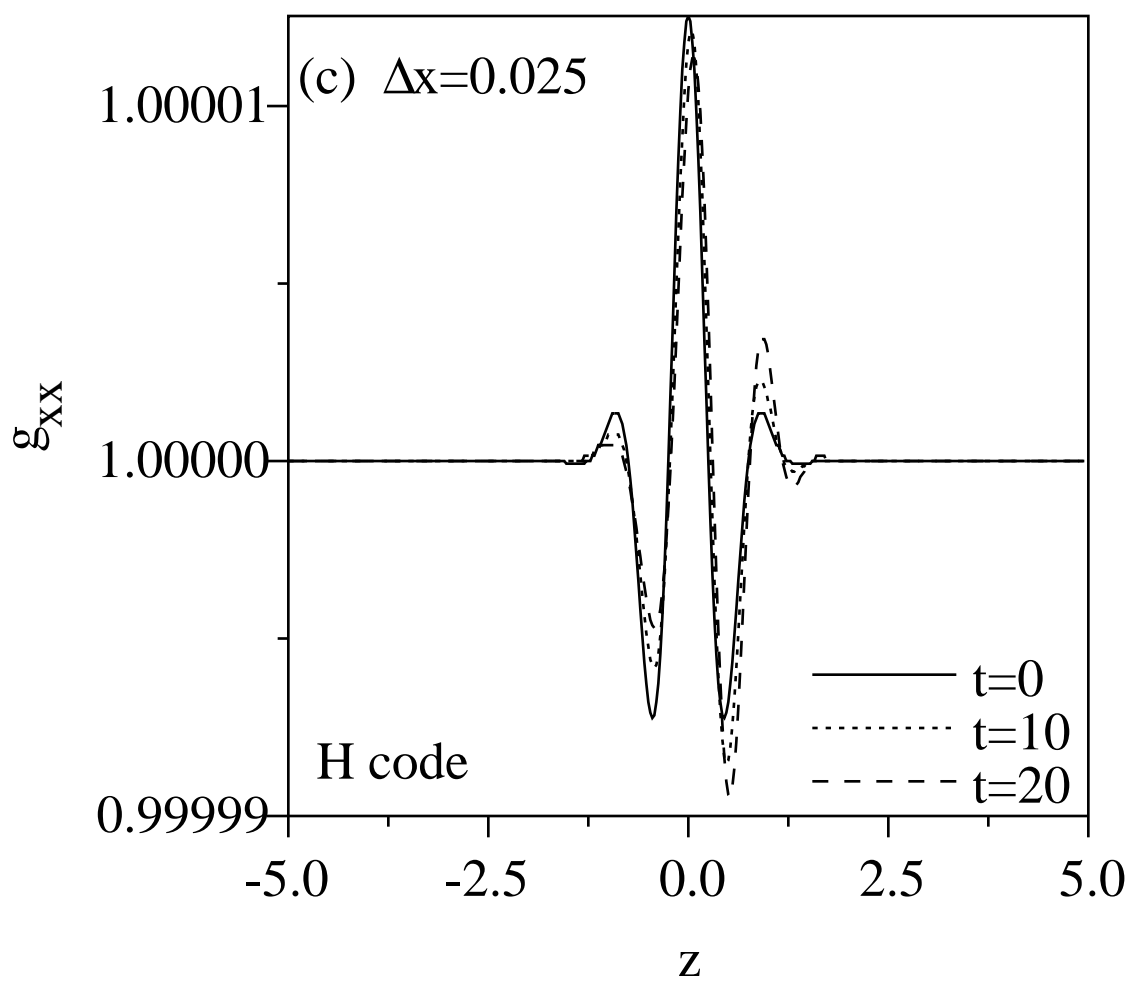


Fig. 2c

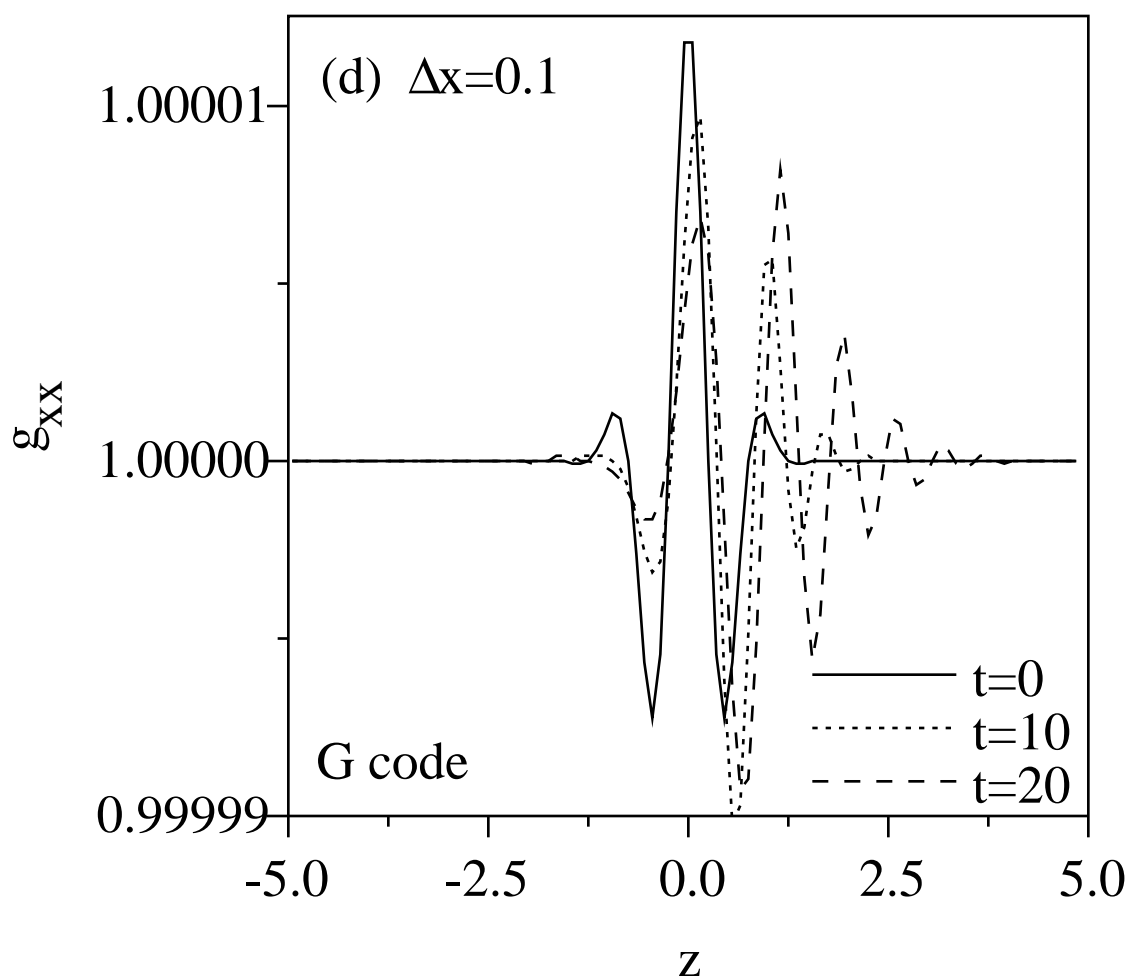


Fig. 2d

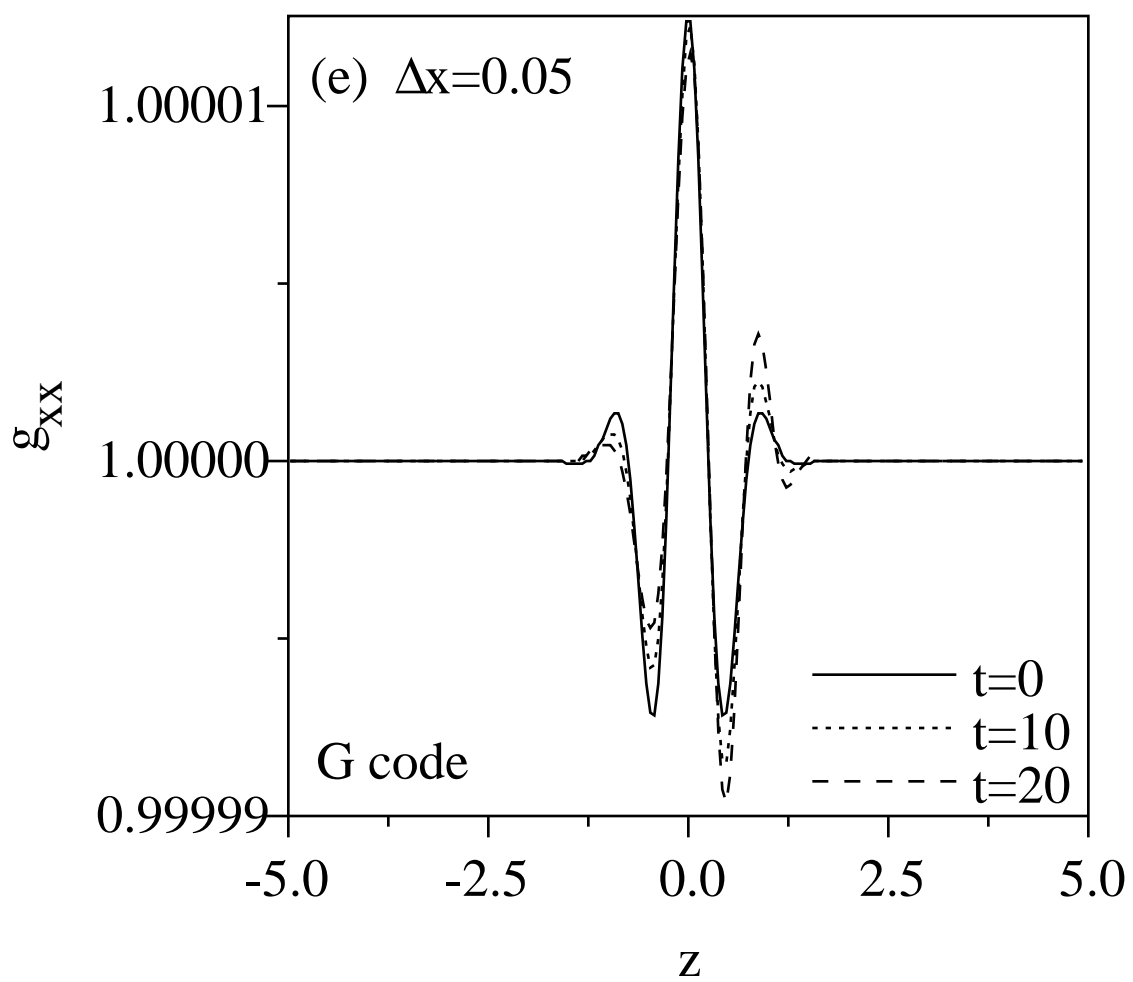


Fig. 2e

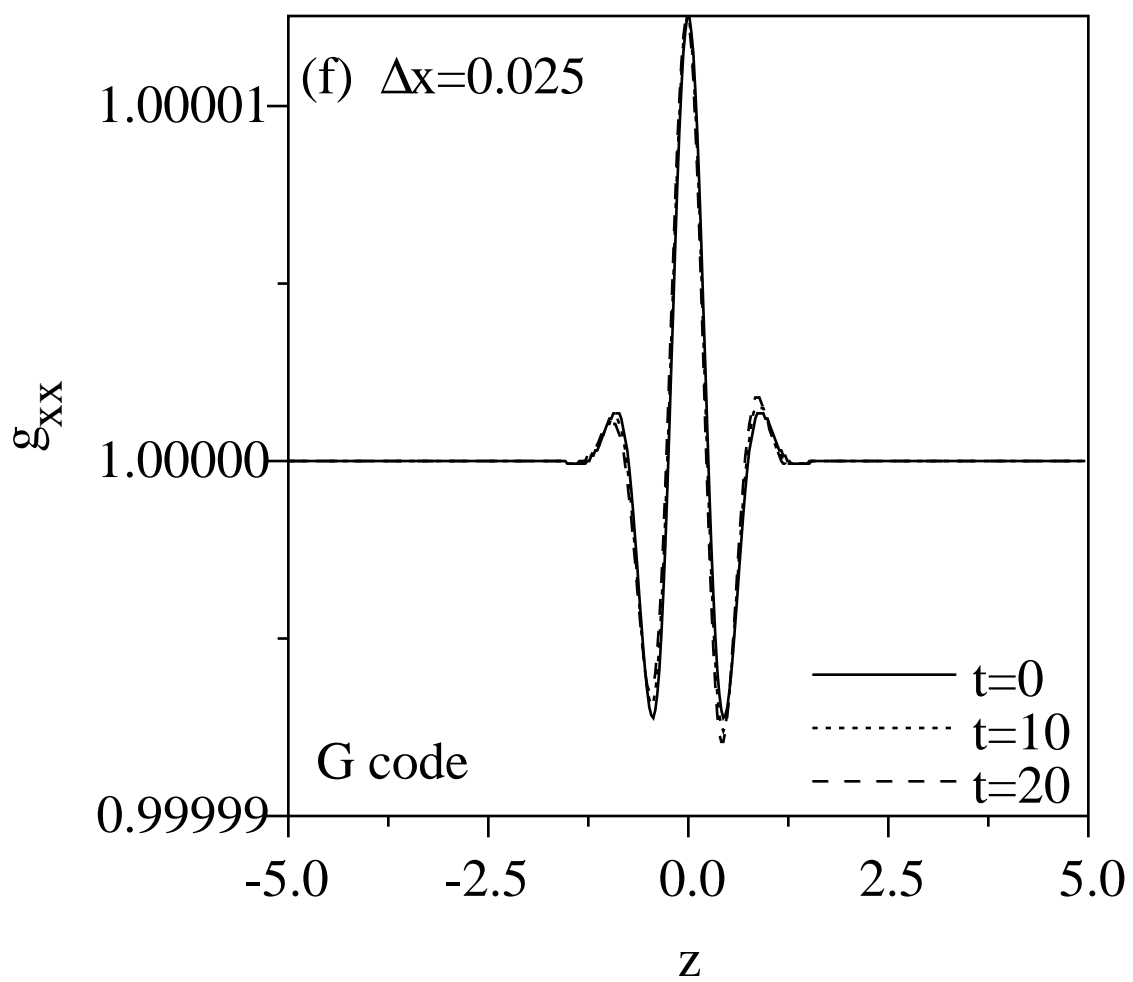


Fig. 2f

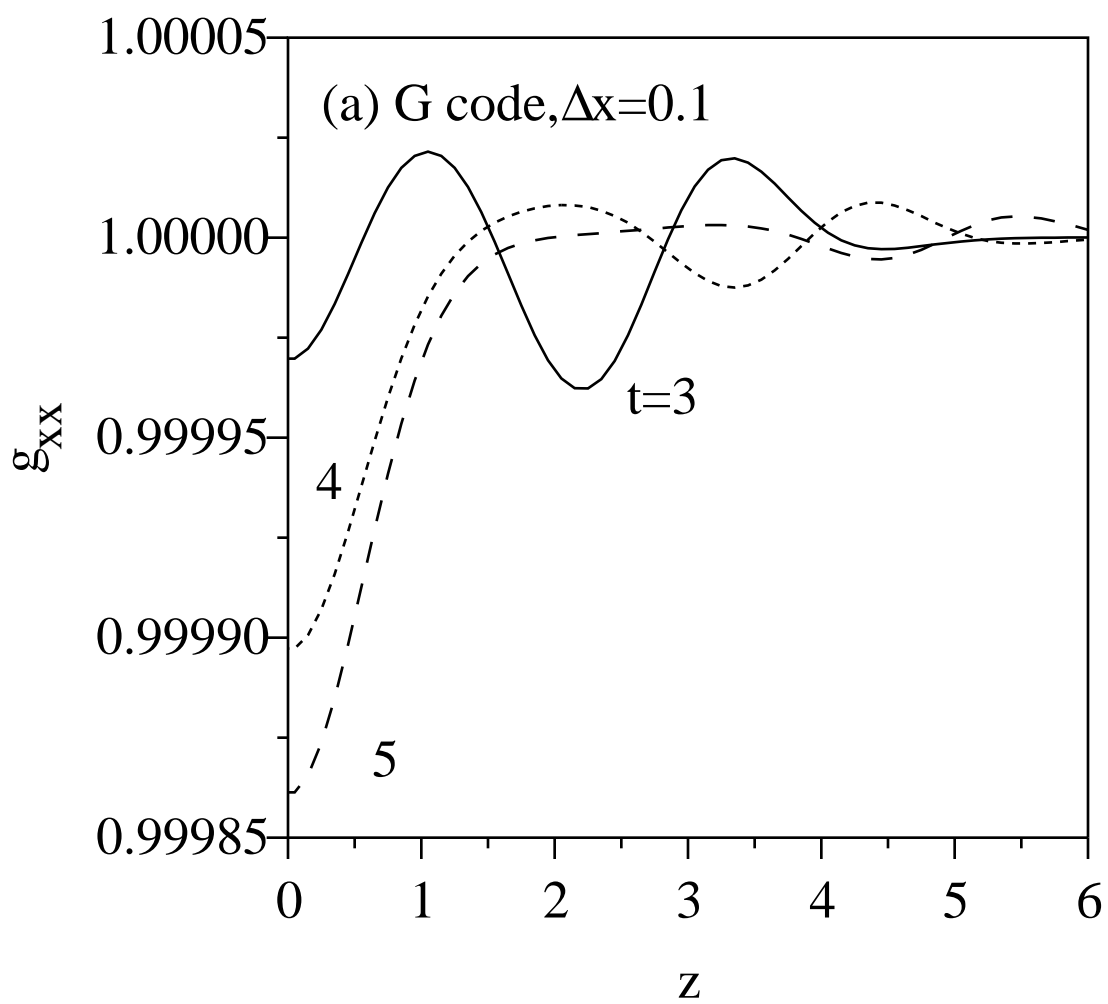


Fig. 11a

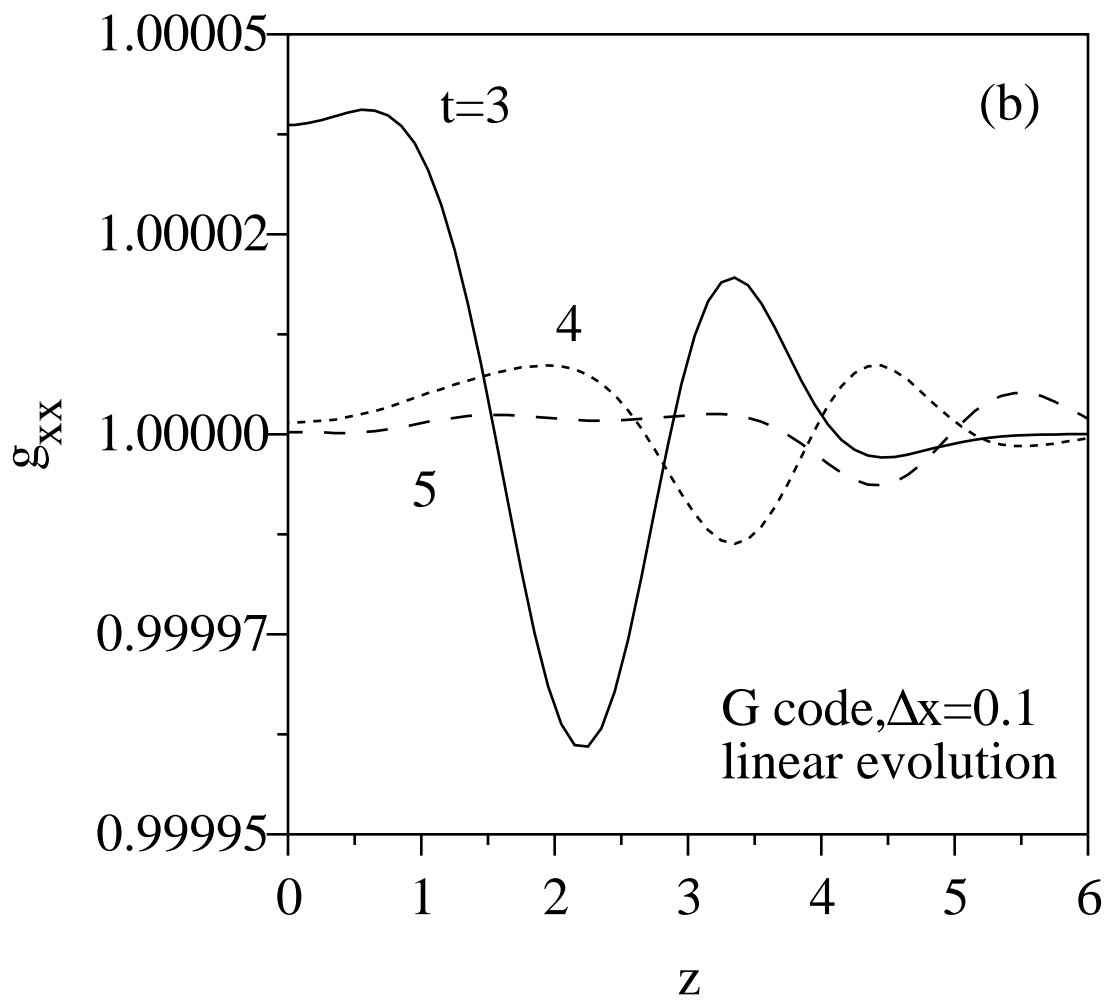


Fig. 11b

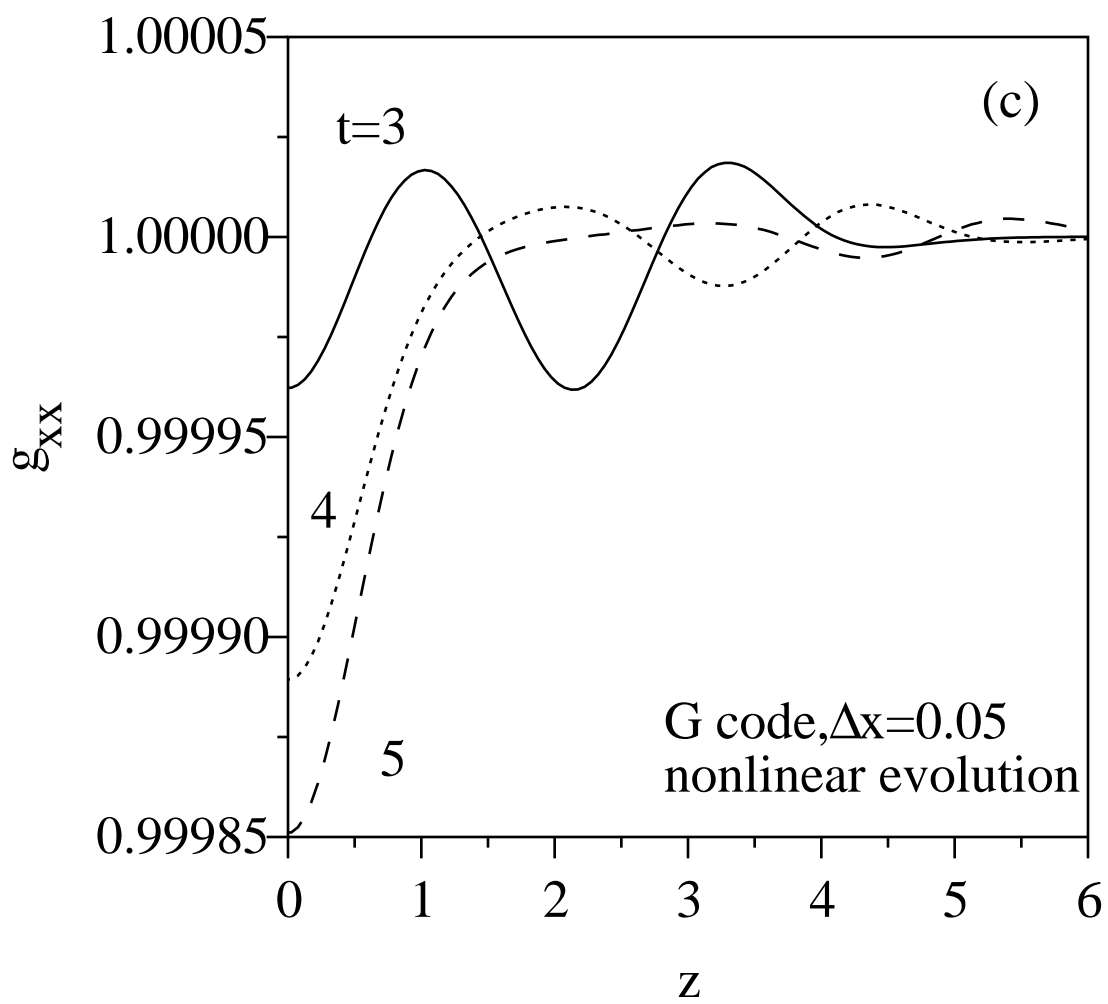


Fig. 11c

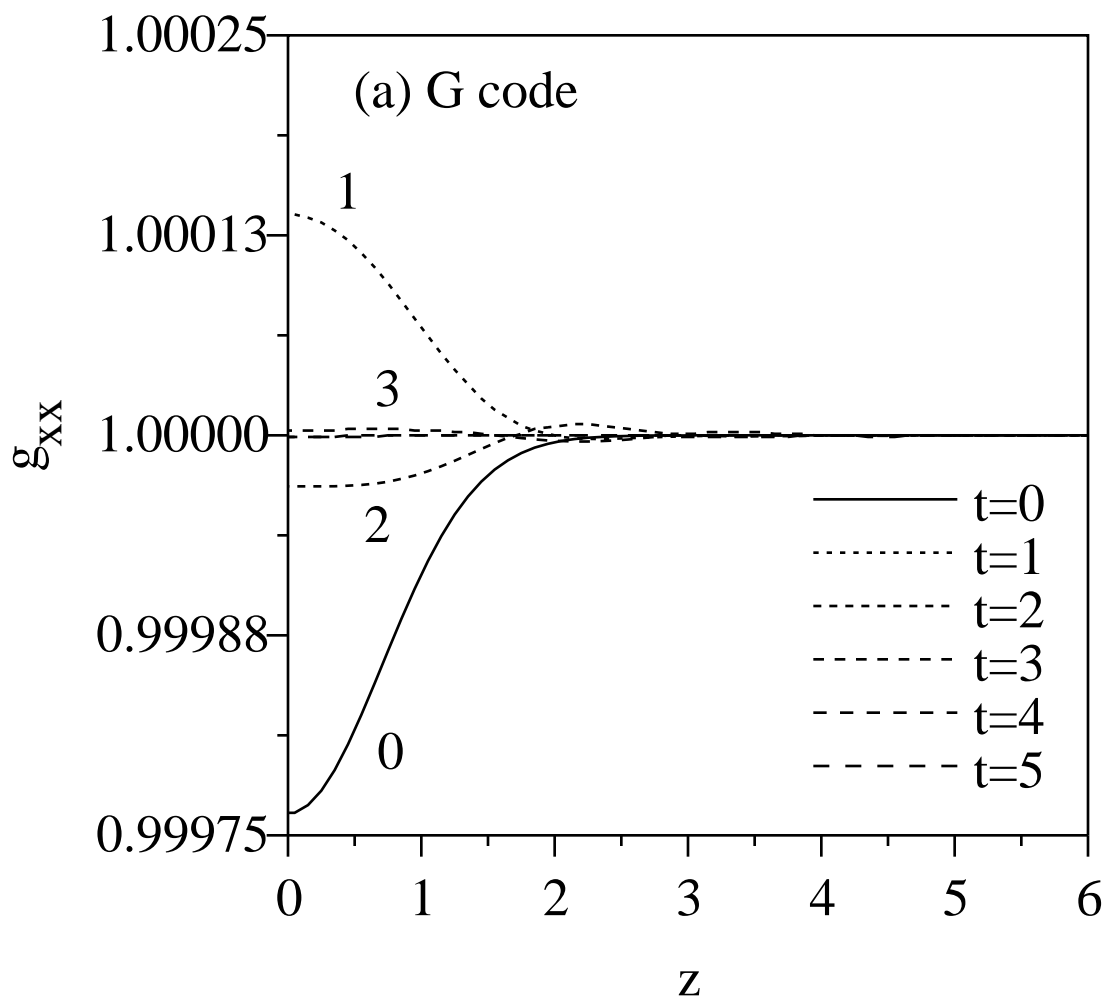


Fig. 9a

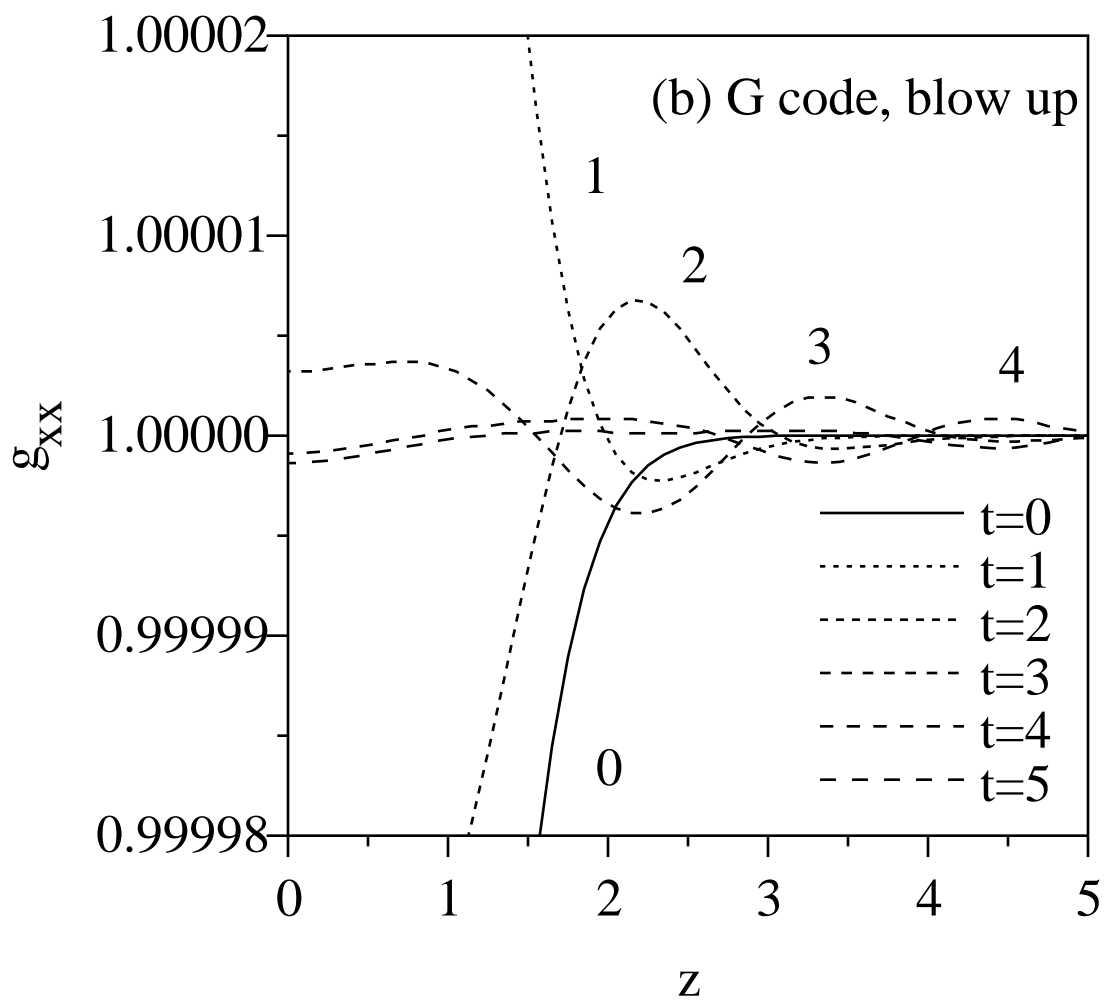


Fig. 9b

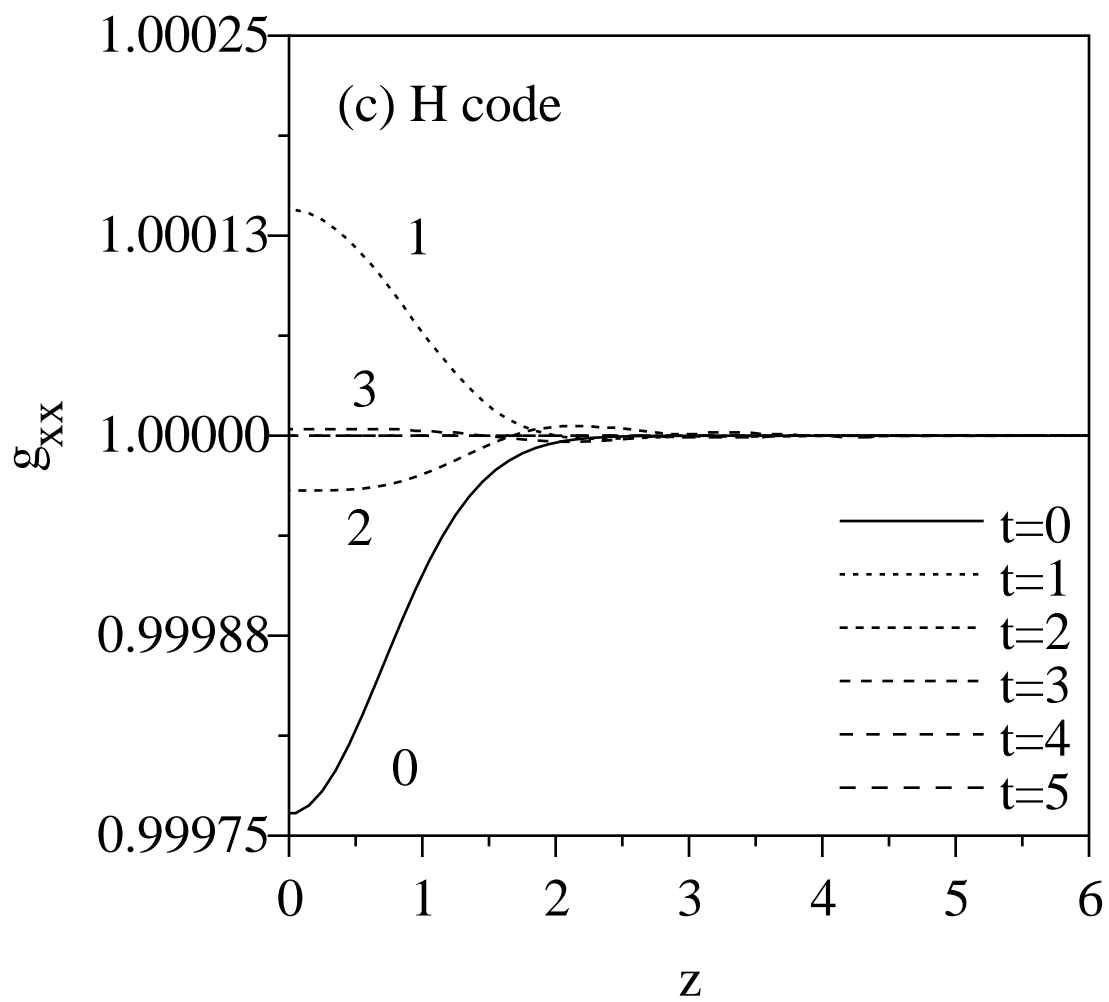


Fig. 9c

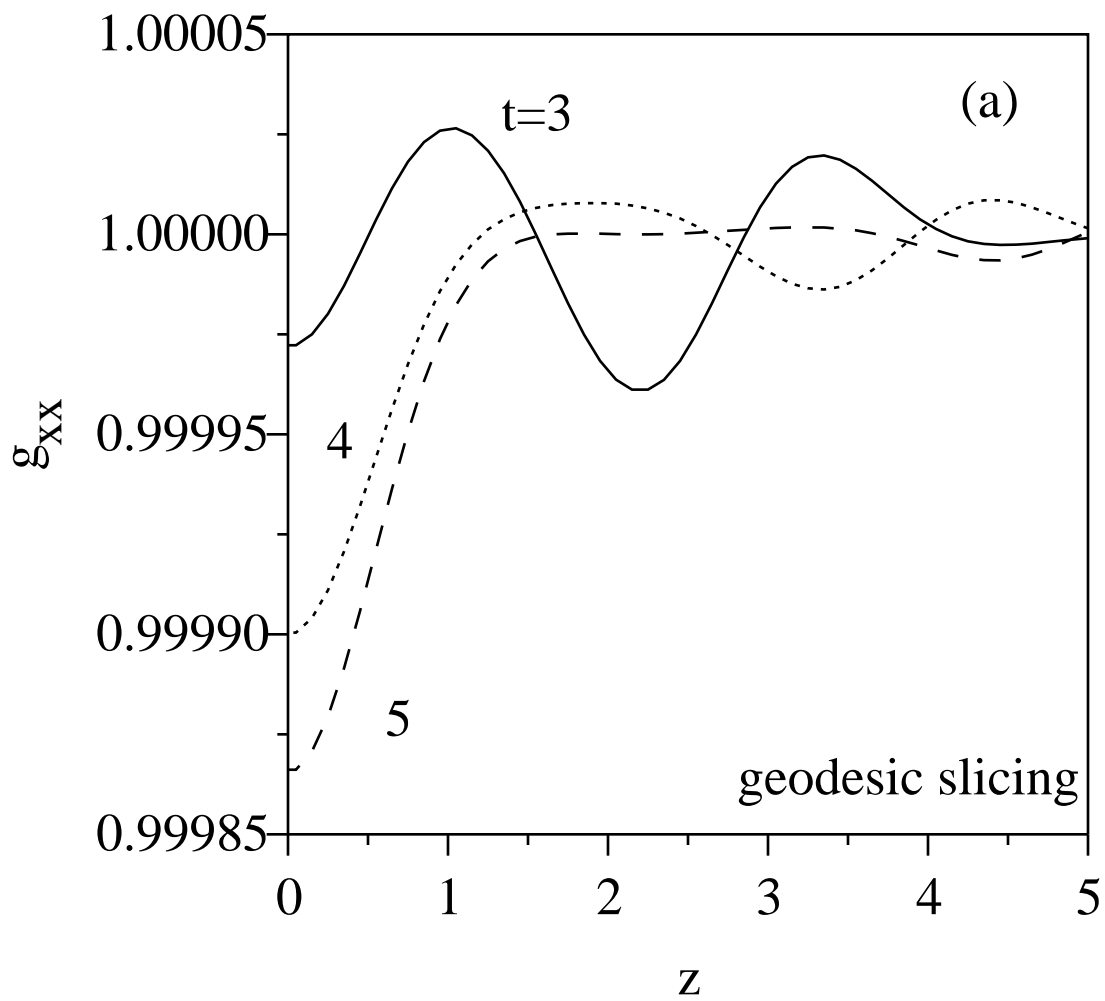


Fig. 13a

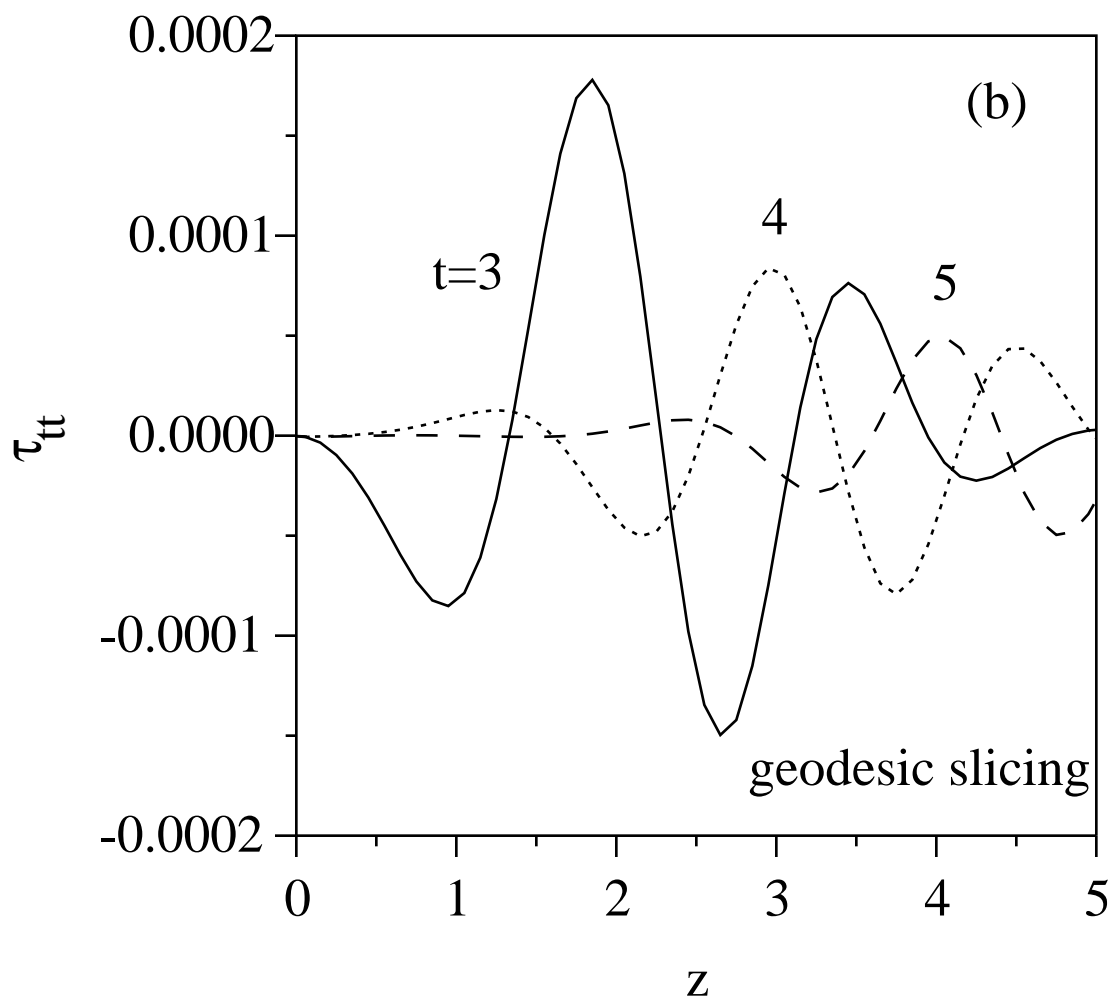


Fig. 13b

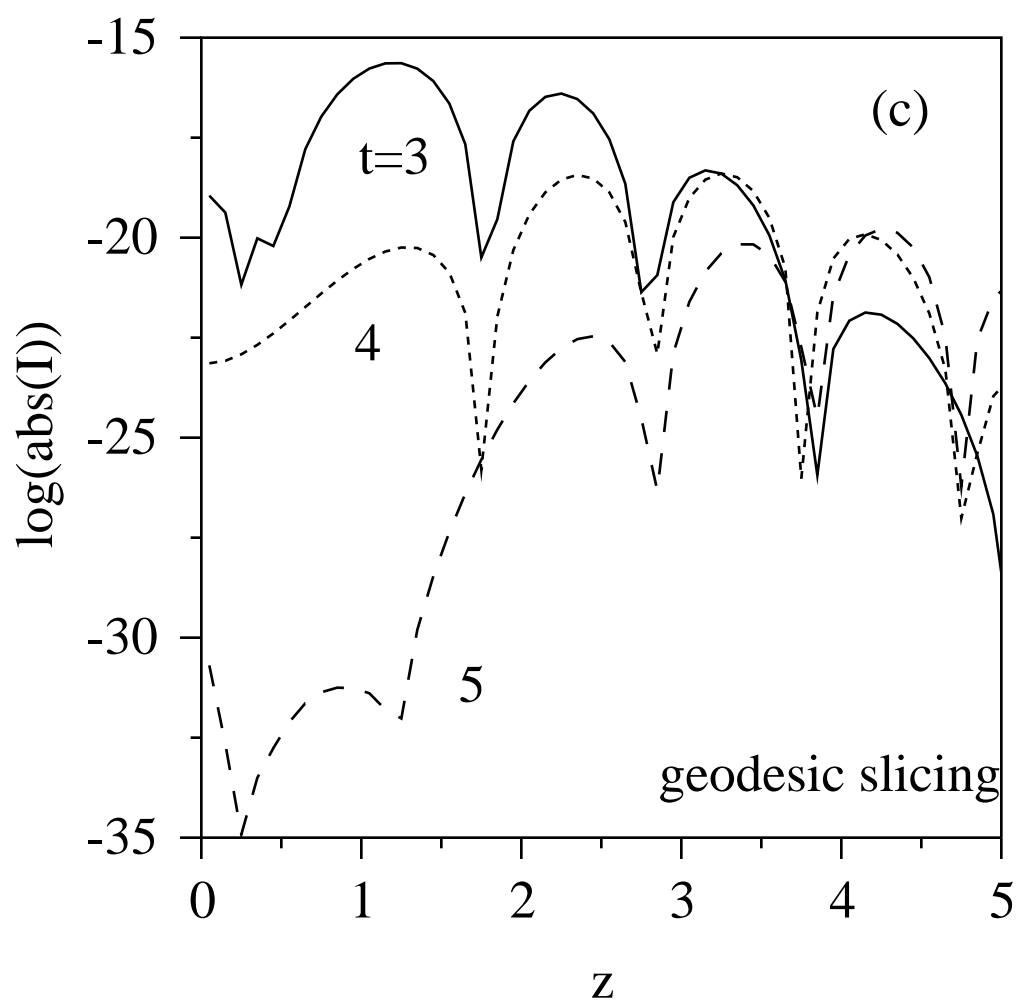


Fig. 13c

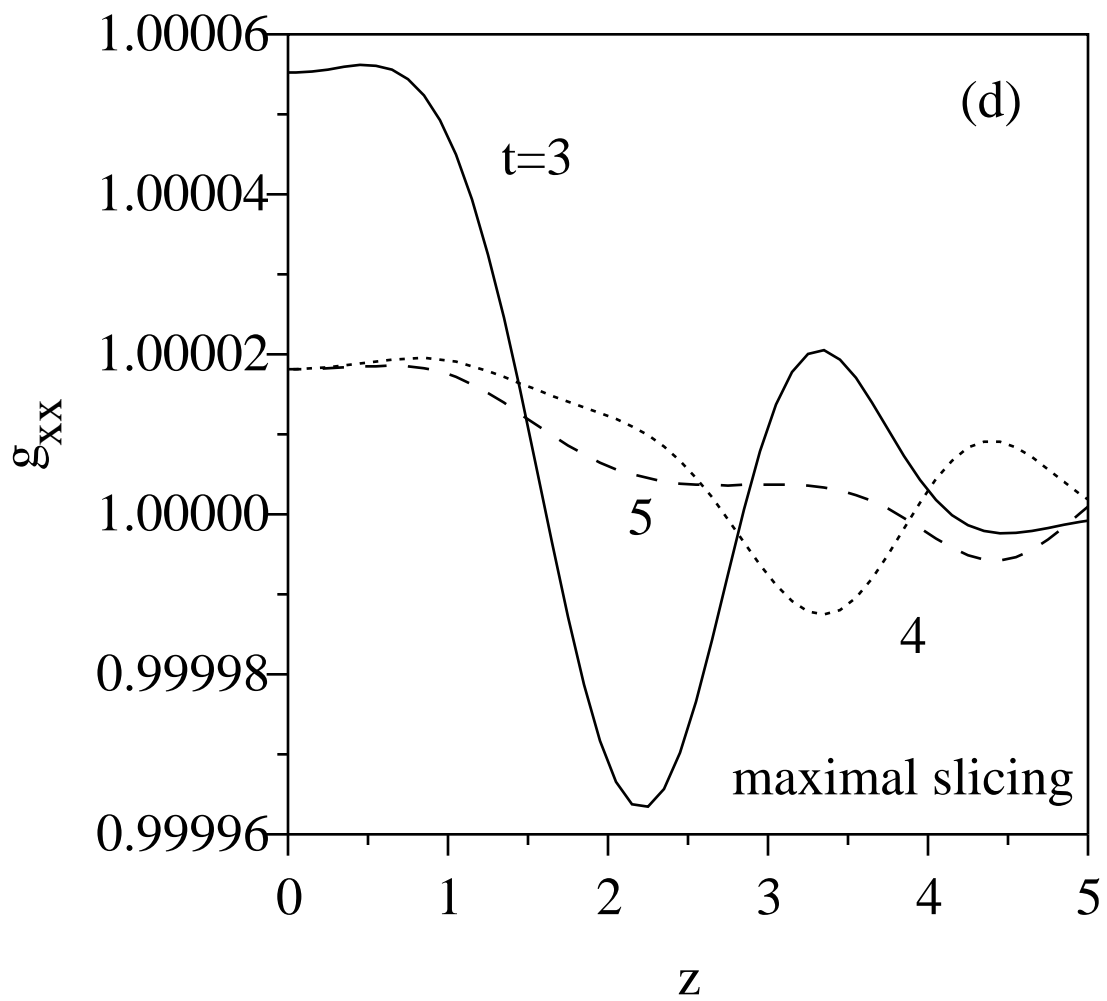


Fig. 13d

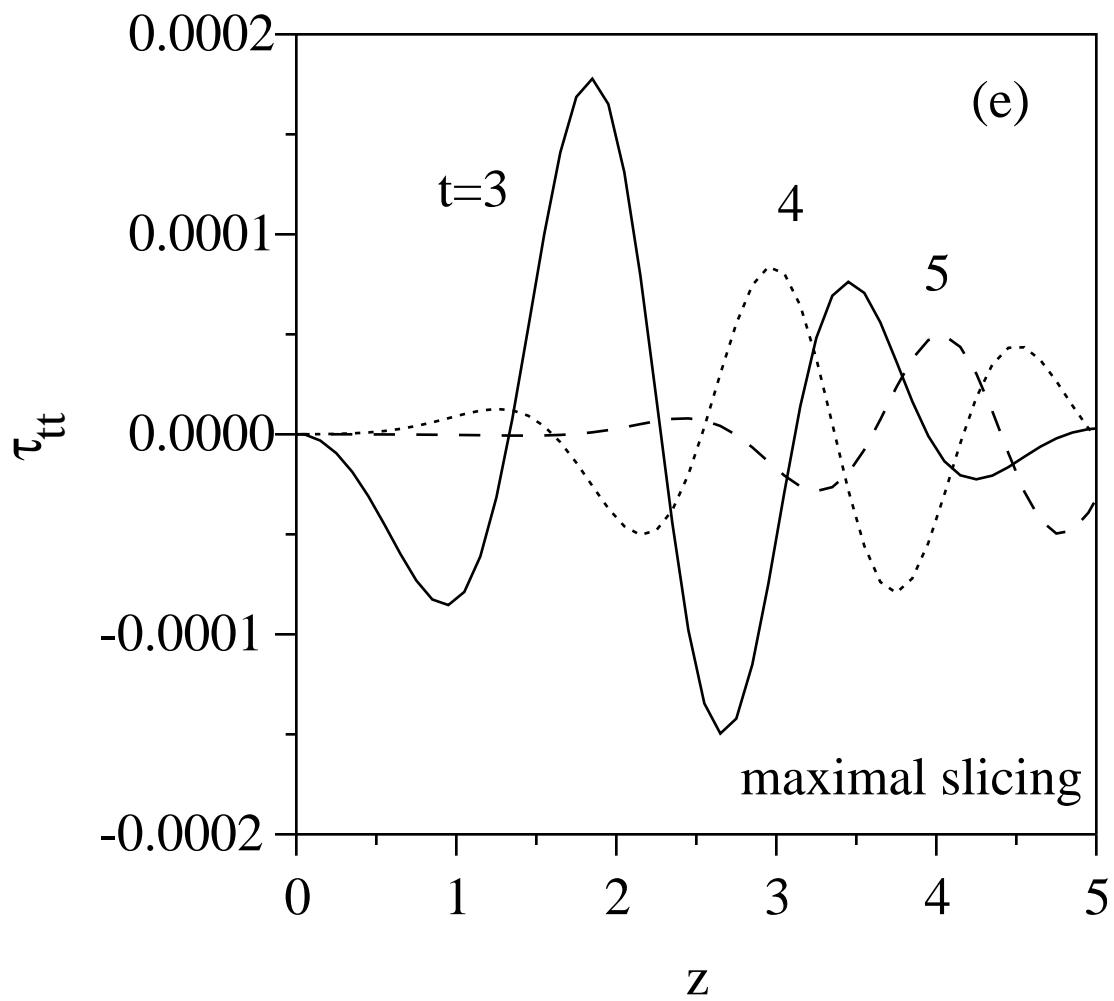


Fig. 13e

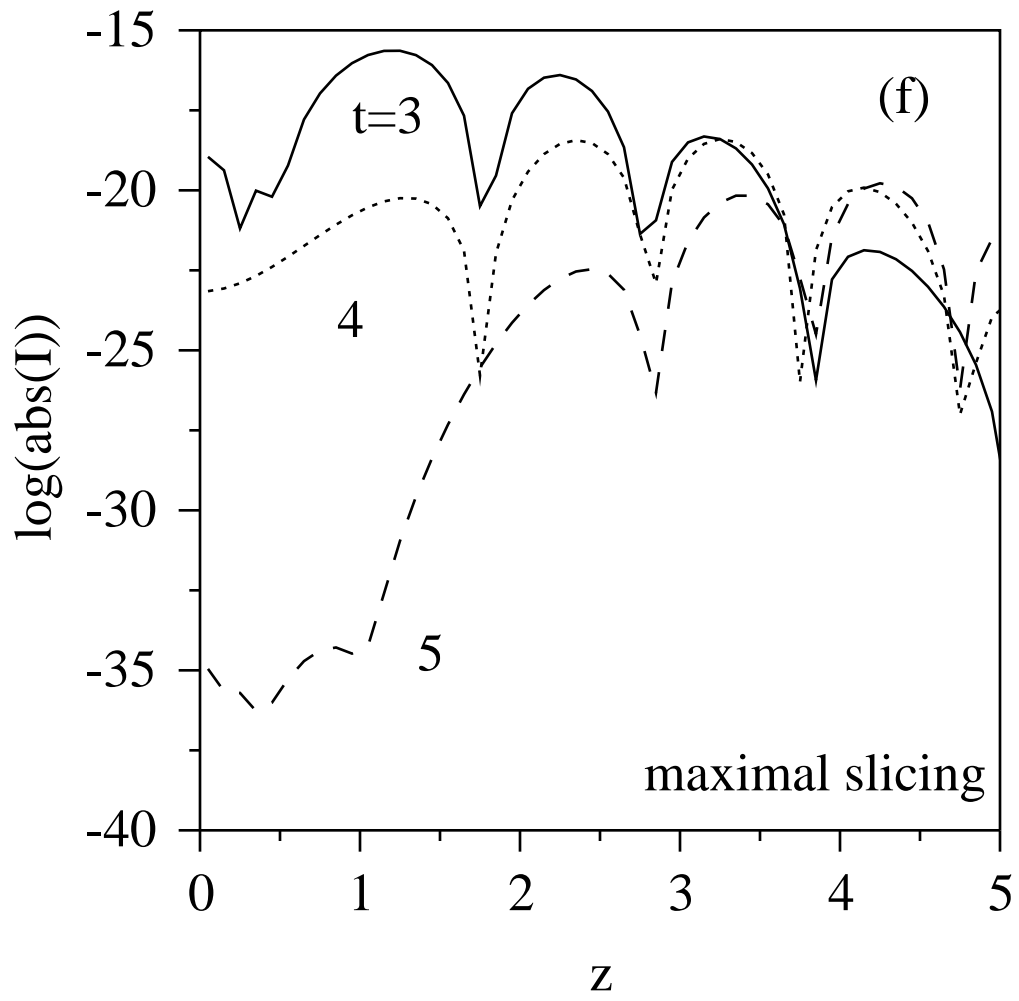


Fig. 13f

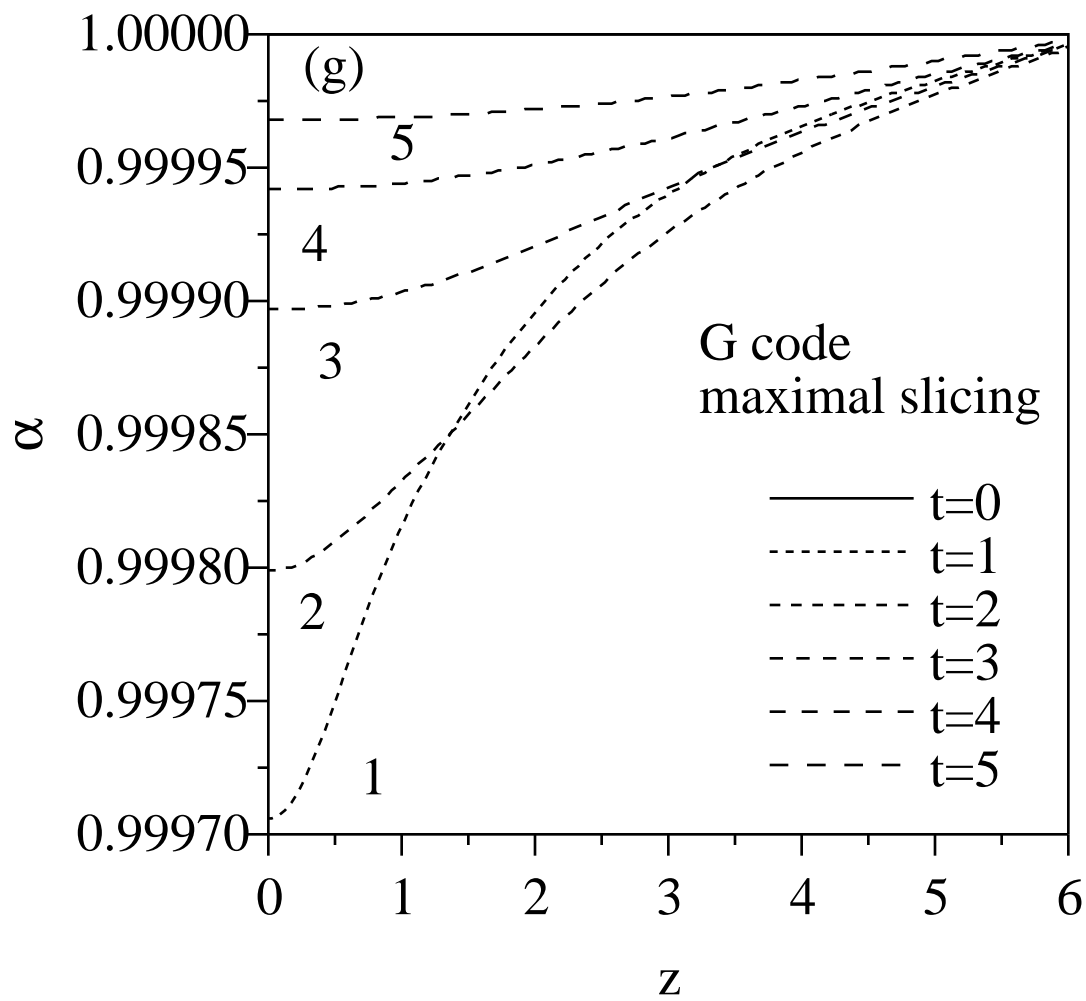


Fig. 13g

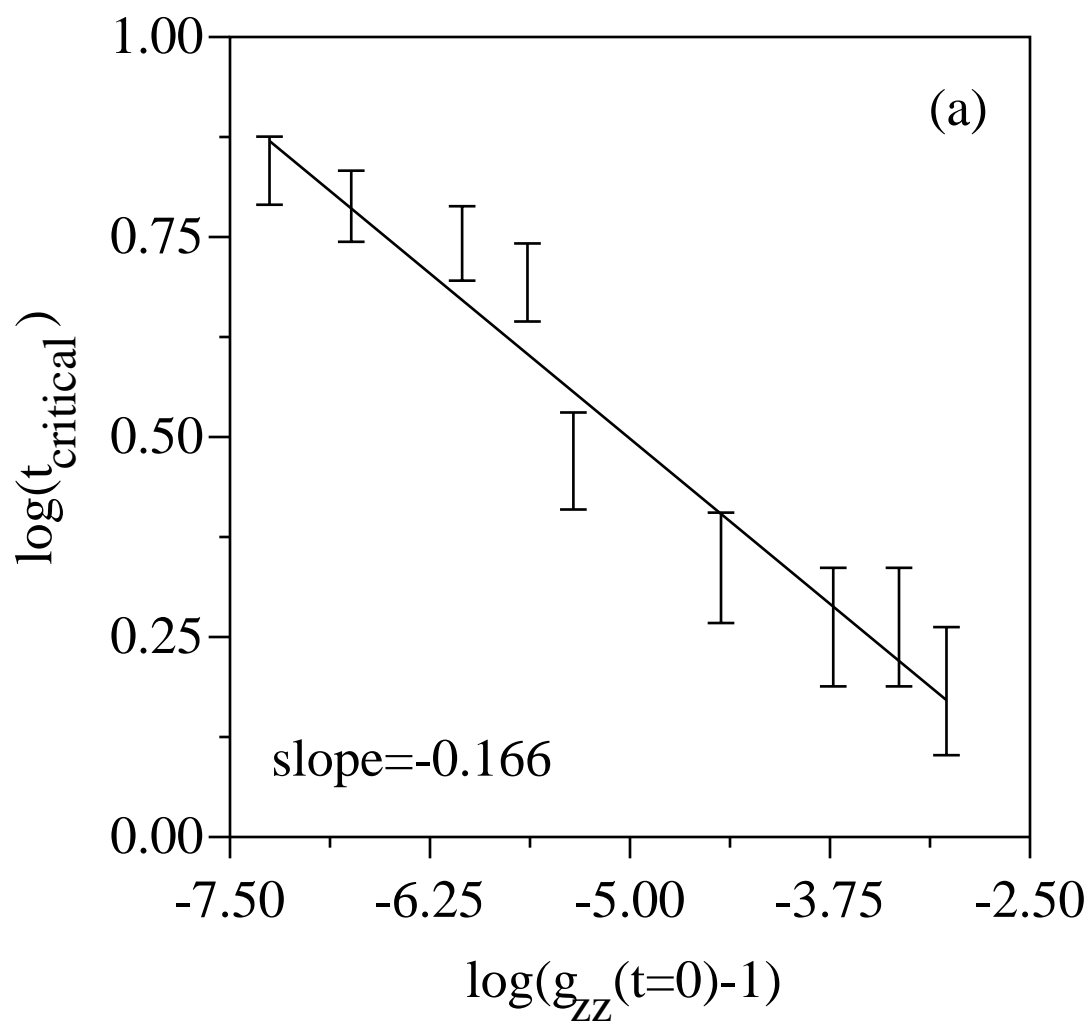


Fig. 14a

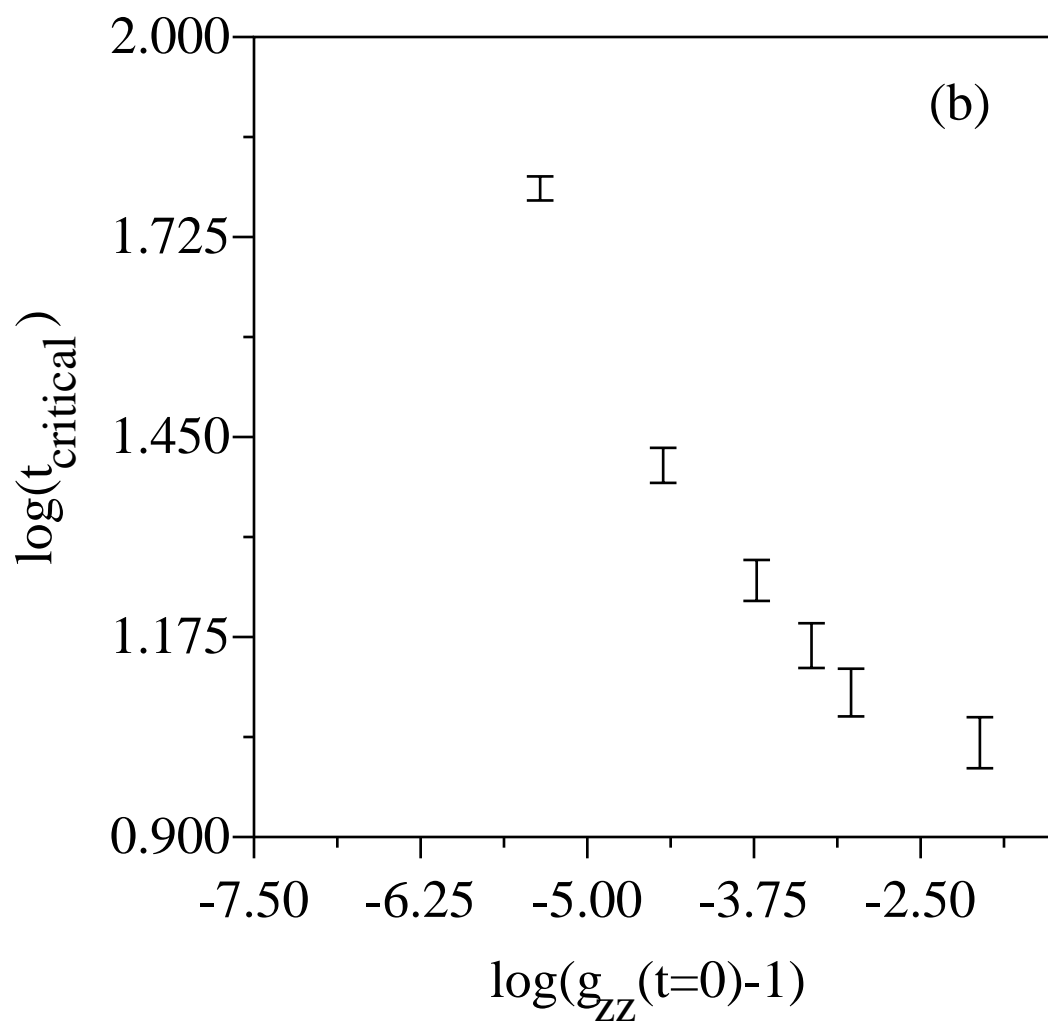


Fig. 14b